

Mixing of counterpropagating signals in a traveling-wave Josephson device

M. Praquin,¹ V. Lienhard,^{1,2} A. Giraudo,¹ A. Vanselow,¹ Z. Leghtas,¹ P. Campagne-Ibarcq¹

¹ *Laboratoire de Physique de l'École Normale Supérieure,
Mines Paris-PSL, Inria, ENS-PSL, Université PSL,
CNRS, Sorbonne Université, Paris, France*

² *Present address: Ohmori Group, Okazaki, Japan*

(Dated: July 1, 2024)

Light waves do not interact in vacuum, but may mix through various parametric processes when traveling in a nonlinear medium. In particular, a high-amplitude wave can be leveraged to frequency convert a low-amplitude signal, as long as the overall energy and momentum of interacting photons are conserved. These conditions are typically met when all waves propagate in the medium with identical phase velocity along a particular axis. In this work, we investigate an alternative scheme by which an input microwave signal propagating along a 1-dimensional Josephson metamaterial is converted to an output wave propagating in the opposite direction. The interaction is mediated by a pump wave propagating at low phase velocity. In this novel regime, the input signal is exponentially attenuated as it travels down the device. We exploit this process to implement a robust on-chip microwave isolator that can be reconfigured into a reciprocal and tunable coupler. The device mode of operation is selected *in situ*, along with its working frequency over a wide microwave range. In the 5.5-8.5 GHz range, we measure an isolation over 15 dB on a typical bandwidth of 100 MHz, on par with the best existing on-chip isolators. Substantial margin for improvement exists through design optimization and by reducing fabrication disorder, opening new avenues for microwave routing and processing in superconducting circuits.

I. INTRODUCTION

Parametric processes are potent and versatile tools in quantum technologies, enabling signal amplification [1, 2], harmonic generation [3], controlled interaction between standing modes [4], non-reciprocal signal transmission [5, 6] and entanglement generation [7], both in the optical and microwave domains. In these processes, input waves mix in a non linear medium to produce output waves such that energy is conserved:

$$\sum_{i=1}^N \epsilon_i \omega_i = 0 \quad (1)$$

where $\epsilon_i = 1$ for input waves $\epsilon_i = -1$ for output waves, ω_i is the frequency of each wave, and the number of involved waves N matches the order of the wave-mixing process. Since the process rate scales as the product of wave amplitudes, a strong *pump* wave (P) is typically employed to enhance interactions between weak *signal* (S) and *idler* (I) waves. When $N = 4$ —which is the case for the $\chi^{(3)}$ medium considered in this work—a pump at frequency $\omega_P = (\omega_S + \omega_I)/2$ is typically employed to activate a two-mode squeezing interaction between the signal and idler waves and induce phase-preserving amplification of an input signal close to the quantum limit. In another mode of operation, a pump at frequency $\omega_P = |\omega_S - \omega_I|/2$ activates a beam-splitting interaction between the waves, converting an input signal to an output idler and vice-versa.

In the first experimental implementations of these ideas, the non linear medium was embedded in a high quality factor resonator in order to enhance interactions [8–15], at the expense of limiting the process working bandwidth. Alternatively, one may send waves through a long section of non linear medium, which is known as a traveling wave parametric process [16–18]. For the interactions along this line to add up construc-

tively, phase-matching must be enforced which results in a second conservation law on momentum

$$\sum_{i=1}^N \epsilon_i k_i = 0, \quad (2)$$

where k_i is the wavevector corresponding to each wave. Thus, the onset of traveling wave parametric amplifiers (TWPAs) allowed for broadband and high dynamic range amplification, at the cost of increased design complexity to ensure that all waves propagate at the same velocity $v_S = v_I = v_P$ [19–38]. Since $\omega_{S,I,P} = v_{S,I,P} k_{S,I,P}$ in that case, conservation laws (1) and (2) are trivially related and phase-matching is enforced.

Traveling wave parametric converters (TWPCs) [39], capable of converting waves from signal to idler frequency, have attracted interest as they are non reciprocal devices: if one reverts the direction of propagation of the signal and idler waves, their propagation velocities $v_{S,I}$ become negative and the now unmatched conversion process is inhibited. Implementing a robust non-reciprocal element with high enough bandwidth and isolation to efficiently route microwave signals is a long standing goal of circuitQED [40–48]. However, TWPCs suffer from the same design complexity as TWPAs and from limited isolation as the non linear medium length and pump amplitude need be precisely adjusted for the conversion from signal to idler to be complete (see Fig 1a).

In this work, we introduce a novel regime of traveling wave conversion where the signal and idler propagate in opposite directions. Phase-matched conversion is achieved in this configuration by lowering significantly the pump wave velocity $|v_P| \ll |v_{I,S}|$ (see Fig 1b). This change of direction of propagation upon conversion drastically changes the waves dynamics : as the idler escapes backward, it cannot be back converted to signal and the signal amplitude decreases

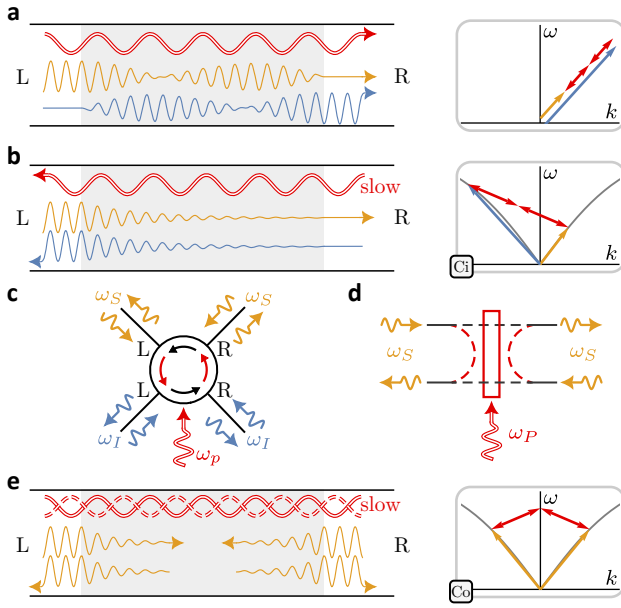


FIG. 1. **Traveling wave parametric conversion.** **a**, In a regular traveling wave device, signal (orange), idler (blue) and pump waves (red) co-propagate in a $\chi^{(3)}$ non-linear medium (gray shaded area), where they mix to coherently convert back and forth signal and idler. Signal isolation is only perfect if the conversion is total at the right port of the device (R). Right panel : in energy-momentum space, waves are represented by arrows arranged in a close form when the process is phase-matched. If all waves propagate with same velocity (aligned arrows), the device is broadband. **b**, In our device, signal and idler waves propagate in opposite directions such that conversion attenuates the signal exponentially. The process is phase-matched by lowering the pump velocity. Right panel : phase-matching is possible at any given signal frequency, irrespective of the exact dispersion relation of the medium (curved gray line), by adjusting the pump frequency. **c**, Signal waves entering from the device left port (L) and idler waves entering from the right port (R) are reflected and frequency converted (red curved arrows) following the process pictured in (b). The same waves entering from the opposite port are transmitted as conversion is not phase-matched in that case, implementing a 4-port circulator (2 physical ports and 2 frequencies of interest). **d**, Our device is reconfigurable into a reciprocal coupler whose transparency is set by the pump amplitude. **e**, This is achieved by feeding the device with pump waves from both ports, generating a standing wave in the nonlinear medium.

exponentially along the line. Moreover, the device may be re-configured to enable controllable reciprocal transmission with high on/off ratio. We now detail these two modes of operation.

On-chip circulation: in this non-reciprocal process, conversion of a signal to an idler photon is enabled by the absorption of 2 photons from a pump wave co-propagating with the idler. The reverse conversion process from idler to signal leads to the emission of 2 photons in the pump wave. The corresponding phase matching diagram is presented in Fig. 1b. From relations 1 and 2, we find the process to be

phase-matched for:

$$\omega_S = 2\omega_P \frac{1/v_I - 1/v_P}{1/v_S - 1/v_I} \quad \omega_I = \omega_S + 2\omega_P \quad (3)$$

where we recall that $v_I, v_P < 0$. Crucially, if one reverses the direction of propagation of both the signal and idler waves, this process is no longer phase-matched and waves propagate unaffected along the transmission line. The device thus circulates signals through 2 frequencies of interest (ω_S and ω_I) at either end of the transmission line, implementing an effective 4-port circulator (see Fig 1c).

Tunable coupling: in this configuration, pump waves of same frequency are applied in both directions. A signal photon may be reflected back to an idler photon of *same frequency* ω_S by absorbing a photon from one of the pump waves and emitting it back in the other (see Fig 1d-e). We find that the process is phase-matched for :

$$\omega_s = \omega_p \left| \frac{v_S}{v_P} \right| \quad \omega_I = \omega_S \quad (4)$$

Since this process is stimulated by pump photons, adjusting the pump amplitudes allows one to continuously tune the effective transmission and reflection coefficients of the line, implementing a tunable coupler.

We note that phase-matching of the target process is straightforward in both configurations as no assumptions are imposed on the relative phase velocities of the propagation modes. It is however exactly verified for a precise set of wave frequencies only. In practice, the operating band of the device (typically of order 100 MHz in our experiment, see section III and supplemental S3) is set by the pump amplitude. Its center frequency is tunable over a wide frequency range by adjusting the pump frequency.

II. DEVICE DESIGN AND CHARACTERIZATION

We design and fabricate a microwave transmission line made of lumped circuit elements and embedding two modes of propagation with different velocities (see Fig 2). Wave-mixing is enabled by Josephson junctions supporting currents from both modes. Note that mixing of counterpropagating signals could also be achieved in a single-mode transmission line if its dispersion relation is properly engineered to slow down the pump wave. Beyond its simple design and wide accordability, our two-mode architecture allows for straightforward separation of the high-amplitude pump wave from the signals to be processed.

In detail, the device is composed of 400 identical cells arranged in series forming two inner electrodes and a ground reference electrode. In each cell, the two inner electrodes are interrupted by two Josephson junctions (inductance $L_J = 0.94$ nH), shunted to ground by two identical parallel-plate capacitors (capacitance $C_g = 0.13$ pF) and connected to each

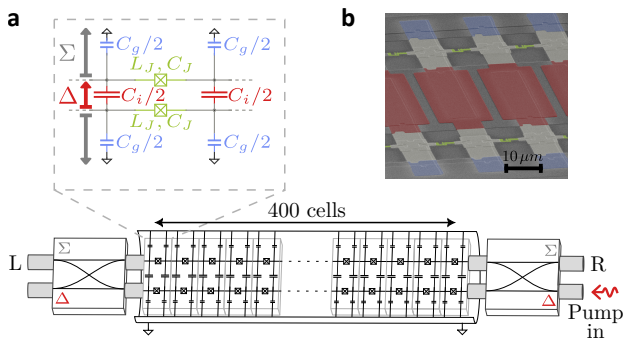


FIG. 2. **Design and fabrication.** **a**, Our device consists of 400 identical cells arranged in series, forming two coplanar superconducting electrodes doped with Josephson junctions (green squared crosses). In each cell, the electrodes are capacitively coupled to each other (red capacitors) and to the ground reference plane (blue capacitors). Given its symmetry, this transmission line embeds two propagation modes with common (Σ) or differential (Δ) phase across the electrodes, both supporting currents through the junctions. Each mode is selectively addressed via hybrid couplers connected at each end of the line. The pump propagates on the Δ mode and is slowed down by the large inner capacitors. The probe signal propagates on the faster Σ mode. **b**, False color scanning electron microscope photograph of the device, see supplemental S8 for details of the fabrication process.

other by a large capacitor ($C_i = 0.57$ pF). The line symmetry ensures that the common and differential excitations of the inner electrodes (labeled Σ and Δ respectively) are eigenmodes of propagation. The large inner capacitor loads the Δ propagation mode—supporting the pump wave—while not affecting the Σ mode—supporting the signal and idler waves of higher velocity. For low-frequency waves, the mode velocities read

$$\begin{aligned} v_{\Sigma,0} &= a/\sqrt{L_J C_g} \\ v_{\Delta,0} &= a/\sqrt{L_J (C_g + 2C_i)} \end{aligned} \quad (5)$$

where a is the unit cell length. We choose the line parameters such that $v_{\Sigma,0}/v_{\Delta,0} \simeq 3$, enabling the target processes in the band 4-10 GHz with a pump tuned from 2.5 GHz to 5 GHz. Remaining parameters are chosen such that waves propagate at approximately constant velocities over the whole frequency range. Indeed, due to the discrete nature of the unit cells, the wave velocity of each mode decreases when approaching a cut-off frequency above which no propagation is possible (see supplemental S3C). Moreover, with our choice of parameters, propagation modes exhibit a characteristic impedance of order 50Ω , allowing us to address them with minimum spurious reflections through a tapered impedance transformer and a hybrid coupler (see supplemental S1 and S2 for details on the wiring setup and transformer geometry).

We may thus probe the Σ mode transmission in presence of a continuous pump wave applied from the right Δ port. In Fig 3, the magnitude of the probe transmission coefficient in each direction is reported in color against the pump frequency ω_{pump} and probe frequency ω_{probe} , exhibiting gaps (blue lines)

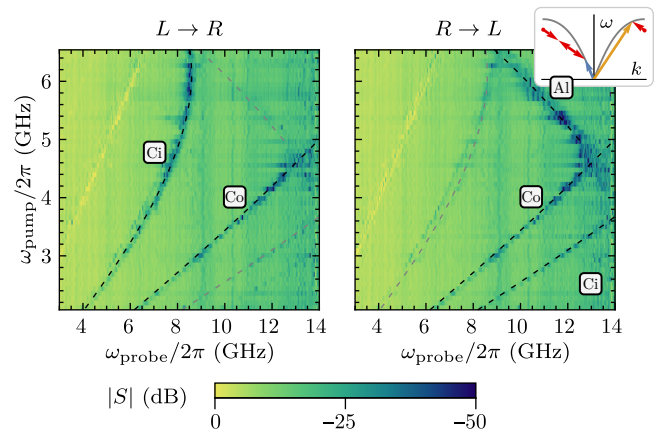


FIG. 3. **Forward and backward transmissions** of a probe applied to the Σ mode in presence of a pump traveling backward on the Δ mode, against pump and probe frequencies. The pump is fed from both ports to improve directionality within the device (see text for details). Gaps in transmission (dark blue) reveal phase-matched processes identified as the circulation (Ci) and tunable coupling (Co) processes of Fig 1b-e, and a process (Al) appearing close to the line cut-off frequency, resulting from aliasing. The location of the gaps is captured with the lumped element model pictured in Fig 2a (dashed lines), see supplemental S3. The depth of the Ci and Al gaps is different in each direction of propagation, showing non-reciprocity. The Co gap should not be visible if the pump was purely unidirectional, indicating internal pump reflection.

when a conversion process is phase-matched. Note that the coherently converted signal may be retrieved by detecting the reflected field at $\omega_{\text{probe}} \pm 2\omega_{\text{pump}}$, which we verified for a few values of ω_{pump} (see supplemental S7). However, the efficiency of the photon flux conversion could not be quantitatively extracted for lack of a precise calibration of the feedlines attenuation at base temperature. This is also the reason for the non-zero baseline attenuation in the data presented in Fig 3, which are only corrected for losses down to the hybrid coupler connecting to the device.

The circulation process, denoted by a marker Ci on the maps, corresponds to the leftmost feature in the left to right transmission (signal to idler upconversion in Fig. 1b) and to the bottom feature in right to left transmission (reverse idler to signal downconversion). Due to the discreteness of the device unit cells, these features curve at high frequency, as expected from the dispersion of the propagation modes. Moreover, a supplementary gap corresponding to the same circulation process opens at high frequency through aliasing of a signal whose wavevector exceeds π/a where a is the length of a unit cell (top right feature labeled (Al) in right panel, with corresponding phase-matching diagram in inset). Crucially all these features are mostly visible in one direction of propagation only, demonstrating non-reciprocity. We attribute the opening of residual gaps in the opposite direction to spurious reflections of the pump within the device and at its ports. Pump directionality within the device may be improved by sending a second pump, with same frequency,

in the reverse direction (see supplemental S5). The maps in Fig 3 and all data pertaining to the circulation were acquired in presence of this compensation tone. Note that it only leads to a modest improvement of the device performances, which is consistent with the presence of a strong reflective defect near the center of the device (also revealed in time domain reflectometry, see supplemental S4).

The tunable coupling process, denoted by a marker (Co) on the maps, corresponds to the central feature visible in both panels. It should not appear if the pump was purely unidirectional, indicating that the pump compensation used to acquire the maps is not fully effective. All data pertaining to the tunable coupling process presented in section III was not acquired by purposely applying a pump in both directions, but rather relying on internal reflections of a pump applied from a single port of the device. Note that the gaps are clearly visible in both directions of propagation, as expected from a reciprocal process.

The location of all gaps corresponding to the circulation and tunable coupling processes is accurately predicted (black dashed lines for expected gaps, gray dashed lines for residual gaps in the reverse transmission) by solving the phase-matching relations 1 and 2 (see S3C). In this model, we take into account the discrete nature of the line unit cells and only leave as free fit parameters the wave velocities at low frequency—found to be within a few percent of their nominal design values—and the Josephson junctions plasma frequency at 38.0 GHz. Note that the origin of a peak in the transmissions at $\omega_{\text{probe}} = \omega_{\text{pump}}$ (appearing as a yellow line in the color maps) and a thin gap lying close to one of the circulation process gaps (visible left of the gray dashed line on the right panel) remains unknown at this stage. We believe the proximity of the latter unknown process to the target circulation process to be coincidental and a result of our specific choice of circuit parameters.

III. DEVICE PERFORMANCES

We further characterize our device performances for non-reciprocal isolation and tunable coupling by recording the probe attenuation in both directions as a function of the applied pump amplitude (Fig 4). The attenuation is obtained, for a given pump amplitude and frequency, by smoothing the probe transmission spectrum over a 40 MHz window around the gap frequency and extracting its maximum depth (see inset of Fig 4a for a typical spectrum before smoothing).

In Fig 4a, we report the attenuation measured for each process at a probe frequency of 7.8 GHz and for a varying pump amplitude, referred by its voltage at room temperature. The low-frequency circulation process (labeled (Ci) in Fig 3 forward transmission) is activated by a pump at 4.63 GHz. It yields a desired attenuation from the left to right port (dark red circles) and a residual attenuation in the opposite direction resulting from pump reflection (light red diamonds). The

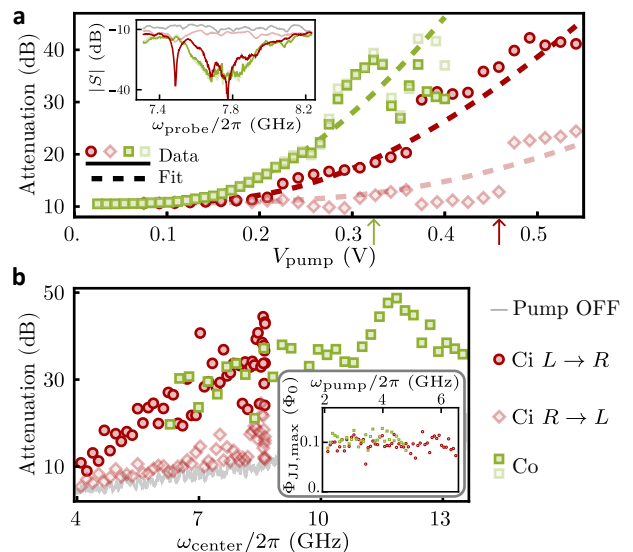


FIG. 4. **Device performances.** **a**, Measured probe attenuation in each direction at $\omega_{\text{center}}/2\pi = 7.8$ GHz in presence of a pump enabling circulation (red, $\omega_{\text{pump}}/2\pi = 4.63$ GHz) or tunable coupling (green, $\omega_{\text{pump}}/2\pi = 2.6$ GHz). For each process, the attenuation and center gap frequency ω_{center} are defined as the depth and position of the gap in the probe transmission (see inset, pump amplitudes chosen to maximize performances indicated by green and red arrows in the main panel), after smoothing over a moving window of 40 MHz. The exponential dependency of each attenuation versus pump amplitude is reproduced by a simple sideband model (dashed lines, see S3) including as single fit parameter the ratio between the room temperature pump amplitude and its value inside the device. **b**, For each pump frequency, we locate the center frequencies of both processes. We adjust the pump amplitudes to maximize performances, and report attenuations versus ω_{center} . **Inset:** estimated maximum phase drop across the device junctions, at the adjusted pump amplitudes, versus pump frequency (see supplemental S3 C 2).

tunable coupling process is activated by a pump at 2.6 GHz, and the corresponding attenuation is reported with green squares. Strikingly, all attenuations scale exponentially with the applied pump amplitude, in agreement with the simple three-wave model presented in Fig 1 and Fig 2. Quantitatively, the predicted attenuation reads $2e^{-\alpha L}/(1 + e^{-2\alpha L})$ where L is the total length of the device and the attenuation constant α , whose exact value depends on the considered process, scales quadratically with the traveling pump wave amplitude (see supplemental S3). Fitting the recorded set of attenuations induced by the circulation process (dark and light red dashed lines, see supplemental for details), we estimate the ratio between the applied pump amplitude at room temperature—referenced by its voltage—and the amplitude of pump waves propagating in each direction within the device—referenced in terms of phase difference across the junctions. We thus estimate that, despite the compensation wave applied from the left Δ port, the spurious pump wave propagating from left to right is only 6 dB weaker than the desired pump wave propagating from right to left. The attenuations from the tunable coupling process, recorded in absence of compensation, are independently fitted (green

dashed line). For both processes, the measured attenuations start deviating significantly from the prediction of our model above a critical pump amplitude $\Phi_{JJ,\max} \sim 0.1 \Phi_0$ where Φ_0 denotes the flux quantum (indicated by green and red arrows in Fig 4a).

In Fig 4b, we report the attenuations obtained over a wide range of operating frequencies of the device. For each target frequency, we tune the pump frequency to activate the desired process and adjust its amplitude at critical value. This value is found to be approximately constant over all considered configurations (see inset), suggesting that wave propagation is significantly affected by spurious non linear processes beyond this critical point. We expect this point to be set by the most inductive junctions in the chain in presence of disorder. Overall, our device enables circulation with over 10dB isolation—defined as the ratio of forward to backward attenuation—through the 5-8.5 GHz band, and approximately 20dB in the 7-8.5 GHz band. Employed as a tunable coupler, it reaches an on/off ratio in transmission higher than 20dB in the 7-14 GHz band. Note that the operating range in circulation is limited by the modest electrical length of our device—resulting in performances tailing off towards lower frequencies—and by the line cutoff frequencies—curving the dispersion relation towards higher frequencies. This range could thus be extended by increasing the number of cells in the device and by reducing the value of capacitances and inductances in each cell, which would also increase our device dynamic range, currently limited at -120 dBm, see supplemental S6. Alternatively, one could invert the pump direction and leverage the other circulation processes (labeled Ci and Ai in Fig 3, backward transmission) to enable circulation at higher frequencies. As for the operating range in tunable coupling, it is only limited by the working bandwidth of various microwave components present in our setup (see supplemental S1).

An important figure of merit for a circulator is its insertion loss, corresponding to the right to left attenuation in Fig 4b. Spurious reflections of the pump wave at the -6 to -3 dB level within the device are responsible for 1 to 5 dB of attenuation, as seen from the comparison to the transmission baseline when the pump is off (gray line). Reducing the reflected wave amplitude through improved Josephson junction reproducibility in fabrication would lead to an exponential decrease of this contribution to the insertion loss. Other contributions include losses of the alumina dielectric—accounting for 1 to 3 dB of attenuation assuming tangent losses $\tan \delta \approx 2 \cdot 10^{-3}$ —and losses of the cabling and sample holder that remain post-calibration. A more precise estimate of insertion loss down to the single-photon regime will be sought in a future work.

IV. CONCLUSION AND OUTLOOK

We introduce a novel regime of traveling-wave parametric conversion by which the signal and idler waves propagate in opposite directions. The conversion process is phase-matched

leveraging a slowly propagating pump wave and results in exponential attenuation of incoming signal waves as they travel down the device. The working frequency is tunable over a wide range by adjusting the pump frequency and conversion can be made either reciprocal or non-reciprocal by applying the pump wave either from a single port or from both ports. Remarkably, our implementation based on a two-mode transmission line doped with lumped capacitors and Josephson junctions performs close to state-of-the-art on-chip isolators [43] in terms of bandwidth and isolation, despite the presence of a defect reflecting waves in the middle of the line.

Looking forward, the device performances could substantially improve through better-controlled fabrication, allowing to extend further the transmission line electrical length, to push its cutoff frequencies toward higher values and to increase its dynamic range while limiting spurious reflections. Alternative designs based on flux-pumped split-junctions [49] or three-wave mixing elements [26] will be explored to the same ends and to limit the participation of the dissipative dielectric material in the transmission mode carrying the signal. In terms of applications, robust on-chip isolators and tunable couplers compatible with standard fabrication techniques will benefit intermediate and large-scale superconducting circuit architectures. In particular, the circulation process we investigate in this work could be combined with standard traveling-wave amplification to achieve the long-standing goal of implementing a fully directional quantum limited amplifier [50]. Another exciting application is the simulation of condensed matter in strong magnetic field [51, 52]. Multi-mode superconducting circuits endowed with non reciprocity can thus exhibit non-trivial phases [53, 54], and a two-mode non reciprocal circuit was recently proposed to implement a fully protected qubit [55].

ACKNOWLEDGMENTS

The authors thank Alice & Bob for providing the sample holder used in this experiment, J. Palomo, M. Rosticher, A. Pierret and J-L. Smirr for assistance in fabrication, and F. Lecocq, M. Malnou and N. Roch for fruitful discussions. This work has been funded by the European Research Council (ERC) under the European Union’s Horizon 2020 research and innovation program (grant agreement No. 101042304), by the French ANR-22-PETQ-0003 grant and by the ANR-22-PETQ-0006 grant under the ‘France 2030’ plan.

COMPETING INTERESTS

M.P. and P.C-I. are inventors of a patent related to the subject.

DATA AVAILABILITY

The experimental data and numerical simulations presented in this manuscript are available from the corresponding authors upon request.

AUTHOR CONTRIBUTIONS

M.P. fabricated the sample, performed the experiment and analyzed the data under the supervision of P.C-I. All authors contributed in designing the experiment and preparing the manuscript.

CORRESPONDENCE

Any correspondence should be addressed to philippe.campagne-ibarcq@inria.fr.

-
- [1] Hansryd, J., Andrekson, P., Westlund, M., Li, J. & Hedekvist, P.-O. Fiber-based optical parametric amplifiers and their applications. *IEEE Journal of Selected Topics in Quantum Electronics* **8**, 506–520 (2002).
- [2] Eom, B. H., Day, P. K., Leduc, H. G. & Zmuidzinas, J. A wide-band, low-noise superconducting amplifier with high dynamic range. *Nature Physics* **8** (2012).
- [3] Efimov, A. et al. Phase-matched third harmonic generation in microstructured fibers. *Optics Express* **11**, 2567 (2003).
- [4] Lecocq, F. et al. Nonreciprocal microwave signal processing with a field-programmable josephson amplifier. *Physical Review Applied* **7**, 024028 (2017).
- [5] Kamal, A., Clarke, J. & Devoret, M. H. Noiseless non-reciprocity in a parametric active device. *Nature Physics* **7**, 311–315 (2011).
- [6] Abdo, B. et al. Full coherent frequency conversion between two propagating microwave modes. *Physical Review Letters* **110**, 173902 (2013).
- [7] Kwiat, P. G. et al. New high-intensity source of polarization-entangled photon pairs. *Physical Review Letters* **75**, 4337–4341 (1995).
- [8] Yamamoto, T. et al. Flux-driven josephson parametric amplifier. *Applied Physics Letters* **93** (2008).
- [9] Bergeal, N. et al. Phase-preserving amplification near the quantum limit with a josephson ring modulator. *Nature* **465**, 64–68 (2010).
- [10] Roch, N. et al. Widely tunable, nondegenerate three-wave mixing microwave device operating near the quantum limit. *Physical Review Letters* **108**, 147701 (2012).
- [11] Mutus, J. Y. et al. Design and characterization of a lumped element single-ended superconducting microwave parametric amplifier with on-chip flux bias line. *Applied Physics Letters* **103** (2013).
- [12] Mutus, J. Y. et al. Strong environmental coupling in a josephson parametric amplifier. *Applied Physics Letters* **104** (2014).
- [13] Eichler, C. & Wallraff, A. Controlling the dynamic range of a josephson parametric amplifier. *EPJ Quantum Technology* **1**, 2 (2014).
- [14] Roy, T. et al. Broadband parametric amplification with impedance engineering: Beyond the gain-bandwidth product. *Applied Physics Letters* **107** (2015).
- [15] Sivak, V. et al. Kerr-free three-wave mixing in superconducting quantum circuits. *Physical Review Applied* **11**, 054060 (2019).
- [16] Cullen, A. L. A travelling-wave parametric amplifier. *Nature* **181**, 332–332 (1958).
- [17] Tien, P. K. Parametric amplification and frequency mixing in propagating circuits. *Journal of Applied Physics* **29**, 1347–1357 (1958).
- [18] Yaakobi, O., Friedland, L., Macklin, C. & Siddiqi, I. Parametric amplification in josephson junction embedded transmission lines. *Physical Review B* **87**, 144301 (2013).
- [19] Castellanos-Beltran, M. A., Irwin, K. D., Hilton, G. C., Vale, L. R. & Lehnert, K. W. Amplification and squeezing of quantum noise with a tunable josephson metamaterial. *Nature Physics* **4**, 929–931 (2008).
- [20] Bockstiegel, C. et al. Development of a broadband nbtin traveling wave parametric amplifier for mkid readout. *Journal of Low Temperature Physics* **176**, 476–482 (2014).
- [21] O’Brien, K., Macklin, C., Siddiqi, I. & Zhang, X. Resonant phase matching of josephson junction traveling wave parametric amplifiers. *Physical Review Letters* **113** (2014).
- [22] Macklin, C. et al. A near quantum-limited josephson traveling-wave parametric amplifier. *Science* **350** (2015).
- [23] White, T. C. et al. Traveling wave parametric amplifier with josephson junctions using minimal resonator phase matching. *Applied Physics Letters* **106** (2015).
- [24] Bell, M. & Samolov, A. Traveling-wave parametric amplifier based on a chain of coupled asymmetric squids. *Physical Review Applied* **4**, 024014 (2015).
- [25] Vissers, M. R. et al. Low-noise kinetic inductance traveling-wave amplifier using three-wave mixing. *Applied Physics Letters* **108** (2016).
- [26] Zorin, A. B. Josephson traveling-wave parametric amplifier with three-wave mixing. *Physical Review Applied* **6** (2016).
- [27] Adamyan, A. A., de Graaf, S. E., Kubatkin, S. E. & Danilov, A. V. Superconducting microwave parametric amplifier based on a quasi-fractal slow propagation line. *Journal of Applied Physics* **119** (2016).
- [28] Chaudhuri, S. et al. Broadband parametric amplifiers based on nonlinear kinetic inductance artificial transmission lines. *Applied Physics Letters* **110** (2017).
- [29] Zhang, W., Huang, W., Gershenson, M. & Bell, M. Josephson metamaterial with a widely tunable positive or negative kerr constant. *Physical Review Applied* **8**, 051001 (2017).
- [30] Frattini, N. E., Sivak, V. V., Lingenfelter, A., Shankar, S. & Devoret, M. H. Optimizing the nonlinearity and dissipation of a snail parametric amplifier for dynamic range. *Physical Review Applied* **10** (2018).
- [31] Ranzani, L. et al. Kinetic inductance traveling-wave amplifiers for multiplexed qubit readout. *Applied Physics Letters* **113** (2018).

- [32] Miano, A. & Mukhanov, O. A. Symmetric traveling wave parametric amplifier. IEEE Transactions on Applied Superconductivity **29**, 1–6 (2019).
- [33] Planat, L. et al. Photonic-crystal josephson traveling-wave parametric amplifier. Physical Review X **10** (2020).
- [34] Goldstein, S. et al. Four wave-mixing in a microstrip kinetic inductance travelling wave parametric amplifier. Applied Physics Letters **116** (2020).
- [35] Malnou, M. et al. Three-wave mixing kinetic inductance traveling-wave amplifier with near-quantum-limited noise performance. PRX Quantum **2** (2021).
- [36] Ranadive, A. et al. Kerr reversal in josephson metamaterial and traveling wave parametric amplification. Nature Communications **13** (2022).
- [37] Peng, K. et al. Floquet-mode traveling-wave parametric amplifiers. PRX Quantum **3**, 020306 (2022).
- [38] Qiu, J. Y. et al. Broadband squeezed microwaves and amplification with a josephson travelling-wave parametric amplifier. Nature Physics **19** (2023).
- [39] Ranzani, L. et al. Wideband isolation by frequency conversion in a josephson-junction transmission line. Physical Review Applied **8** (2017).
- [40] Kamal, A., Roy, A., Clarke, J. & Devoret, M. H. Asymmetric frequency conversion in nonlinear systems driven by a biharmonic pump. Physical Review Letters **113**, 247003 (2014).
- [41] Metelmann, A. & Clerk, A. Nonreciprocal photon transmission and amplification via reservoir engineering. Physical Review X **5**, 021025 (2015).
- [42] Sliwa, K. et al. Reconfigurable josephson circulator/directional amplifier. Physical Review X **5**, 041020 (2015).
- [43] Chapman, B. J. et al. Widely tunable on-chip microwave circulator for superconducting quantum circuits. Physical Review X **7** (2017).
- [44] Naghiloo, M., Peng, K., Ye, Y., Cunningham, G. & O'Brien, K. P. Broadband microwave isolation with adiabatic mode conversion in coupled superconducting transmission lines. arXiv (2021). URL <http://arxiv.org/abs/2103.07793>.
- [45] Kwende, R., White, T. & Naaman, O. Josephson parametric circulator with same-frequency signal ports, 200 mhz bandwidth, and high dynamic range. Applied Physics Letters **122** (2023).
- [46] Navarathna, R. et al. Passive superconducting circulator on a chip. Physical review letters **130**, 037001 (2023).
- [47] Cao, X., Irfan, A., Mollenhauer, M., Singirikonda, K. & Pfaff, W. Parametrically controlled chiral interface for superconducting quantum devices. arXiv (2024). URL <https://arxiv.org/abs/2405.15086v1>.
- [48] Kumar, N. P., Le, D. T., Pakkiam, P., Stace, T. M. & Fedorov, A. Fano-enhanced low-loss on-chip superconducting microwave circulator (2024). URL <https://arxiv.org/abs/2406.14821v1>.
- [49] Zorin, A. B. Flux-driven josephson traveling-wave parametric amplifier. Physical Review Applied **12** (2019).
- [50] Liu, G. et al. Fully directional quantum-limited phase-preserving amplifier. Physical Review Applied **21**, 014021 (2024).
- [51] Owens, J. C. et al. Chiral cavity quantum electrodynamics. Nature Physics **18**, 1048–1052 (2022).
- [52] Rosen, I. T. et al. Implementing a synthetic magnetic vector potential in a 2d superconducting qubit array. arXiv (2024). URL <https://arxiv.org/abs/2405.00873>.
- [53] Qi, X.-L. & Zhang, S.-C. Topological insulators and superconductors. Reviews of modern physics **83**, 1057 (2011).
- [54] von Klitzing, K. et al. 40 years of the quantum hall effect. Nature Reviews Physics **2**, 397–401 (2020).
- [55] Rymarz, M., Bosco, S., Ciani, A. & DiVincenzo, D. P. Hardware-encoding grid states in a nonreciprocal superconducting circuit. Physical Review X **11**, 011032 (2021).
- [56] Eul, H.-J. & Schiek, B. Thru-match-reflect: One result of a rigorous theory for de-embedding and network analyzer calibration.
- [57] Engen, G. F. & Hoer, C. A. "thru-reflect-line": An improved technique for calibrating the dual six-port automatic network analyzer (1979).
- [58] Clayton, P. Analysis of Multiconductor Transmission Lines, 2E (2007).
- [59] Pozar, D. Microwave Engineering (Wiley, 2012).
- [60] Greco, A. F. G., Barroso, J. J. & Rossi, J. O. Modeling and analysis of ladder-network transmission lines with capacitive and inductive lumped elements. Journal of Electromagnetic Analysis and Applications **05**, 213–218 (2013).
- [61] Keysight. Time domain analysis using a network analyzer.

Supplemental Materials

S1. EXPERIMENTAL SETUP

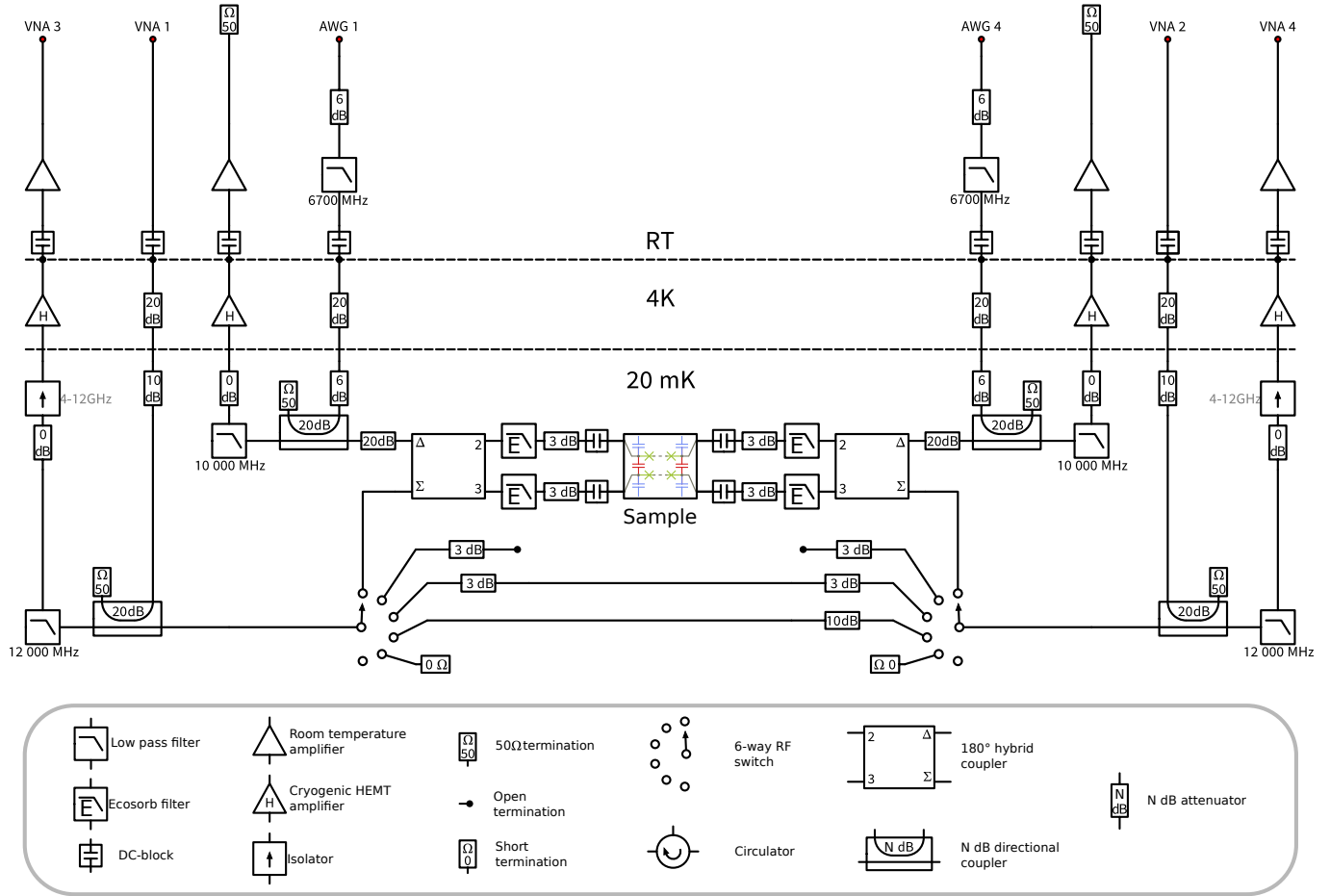


FIG. S1. **Measurement setup.** See text for details.

The sample was measured using a vector network analyzer (VNA, model P5024A from Keysight) in a dilution refrigerator with a base temperature of 10mK. An arbitrary waveform generator (AWG, model M8195A from Keysight, with a sampling rate of 65GSa/s) was used to generate the pump waves, ensuring a spectrally pure wave, with controlled relative phase and harmonics at a level better than -20dBc. The Σ and Δ eigenmodes of the sample are addressed from both sides through 180° hybrid couplers and directional couplers. In practice, the pump is sent through the Δ port of the leftmost hybrid coupler or through the Δ port of each hybrid (depending on circulator or coupler configuration), and the probe tone from the VNA is sent to the Σ port of one or the other hybrid coupler. The sample is held inside layers of mu-metal, aluminum and copper shielding. 3-dB attenuators on each sample port help provide a clean impedance background to the sample. The output lines of the Σ ports are routed through isolators (model LNF-ISIS-C412A from Low Noise Factory) and commercial HEMT amplifiers (model LNF-LNC0.3_14B from Low Noise Factory). The output lines of the Δ ports are routed through a 20dB attenuator instead of an isolator to protect against the amplifier thermal noise, as circulators covering the pump frequency range were not available. Finally, microwave switches on either side of the Σ measurement lines allow to measure calibration standards instead of the sample. The minimal set of reflect, thru and attenuated line standards are present to effectively shift the VNA reference plane to the input of the hybrid couplers Σ ports [56, 57]. It is noteworthy that the post-calibration reference planes are still far from the two-mode Josephson line at the core of the sample: it is a limitation of using a four-port sample addressed through hybrid couplers instead of a two-port sample. Undesirable losses from the filters, hybrid couplers, and long cabling (only 1m cables were available, and connect the sample to the closest DC-blocks) are still present. However, the full in-situ calibration is what allows precise knowledge of the attenuation

and phase of the lines, and in turn accurate time domain reflectometry, see appendix S4. Spectrum analyzer measurements, see appendix S7, were performed by using one of the two VNA ports as a continuous wave source to send the input Σ tone while the analyzer (model SA124B from Signal Hound) is plugged at an output in place of the other VNA port.

S2. DEVICE LAYOUT & IMPEDANCE MATCHING

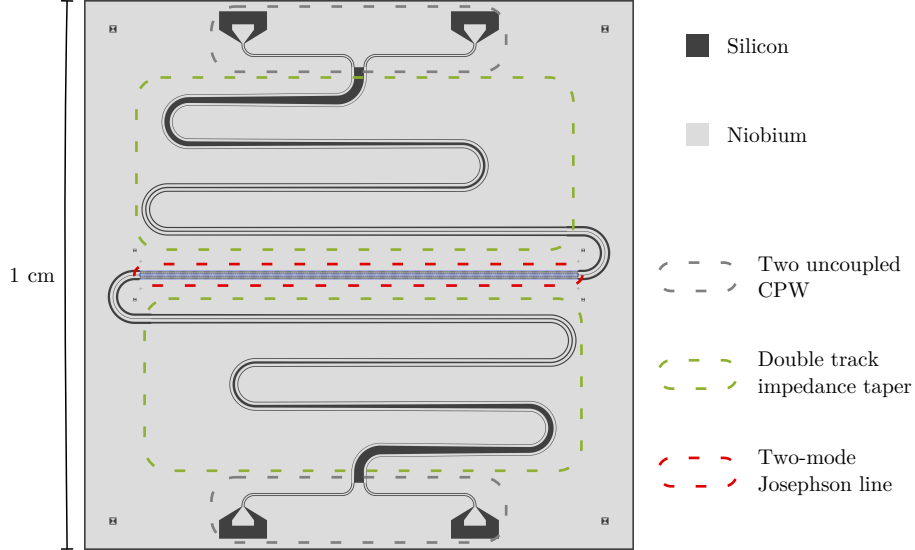


FIG. S2. **The device layout.** We see two launchpads at the top of the chip, and two at the bottom. Starting from two launchpads, two standard CPW lines merge together, at the start of the Klopfenstein impedance taper. The lines are slowly coupled together in the taper, which is meandered for increased length. The taper is then connected to the nonlinear transmission line, in the middle of the sample.

In this section, we describe the device layout, which is constrained by impedance considerations. The device must be connected to the standard 50Ω coaxial lines of the cryostat. However, given the electrical layout of Fig 2e, the lines are coupled, and it is impossible to have both propagating mode impedances at 50Ω at the same time. More precisely, defining the eigenmode voltages and currents as $V_{\Delta} = (V_2 - V_1)/2$, $V_{\Sigma} = (V_2 + V_1)/2$, $i_{\Delta} = (i_2 - i_1)/2$, $i_{\Sigma} = (i_2 + i_1)/2$, the mode impedances are found to be [58]:

$$Z_{\Sigma} = \sqrt{\frac{L_J}{C_g}} \quad (S1)$$

$$Z_{\Delta} = \sqrt{\frac{L_J}{C_g + 2C_i}} \quad (S2)$$

Note that with this Σ/Δ eigenmode convention two identical single mode uncoupled 50Ω lines will, when considered together, have $Z_{\Sigma} = Z_{\Delta} = 50\Omega$.

In our device, we made the choice of L_J , C_g and C_i values so that $\sqrt{Z_{\Sigma}Z_{\Delta}} = 50\Omega$, such that one mode has an impedance slightly above 50Ω ($Z_{\Sigma} = 89\Omega$) and the other slightly below ($Z_{\Delta} = 28\Omega$). We then match both modes to 50Ω simultaneously using a Klopfenstein impedance taper [59]. To achieve this, we slowly vary multiple dimensions of the Ground-Signal-Signal-Ground coplanar waveguides that connect the non-linear transmission line to the launchpads along the length of the taper, see Fig S2. Note that there is an impedance jump caused by the sudden introduction of a middle ground plane, where the multiconductor coupled line parts into two uncoupled coplanar waveguide lines. There is another jump at the other extremity of the taper. This is desired in the specific case of the Klopfenstein taper, see the profile in Fig S3.

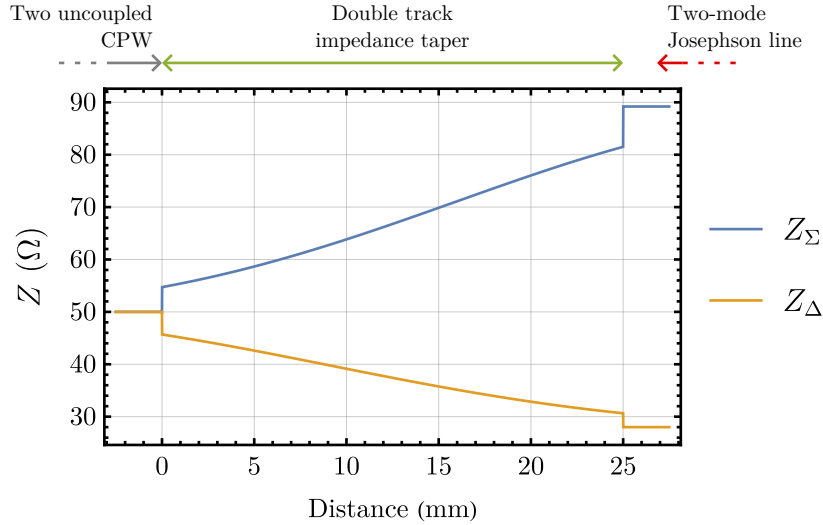


FIG. S3. **Impedance profile of the device Klopfenstein taper** as a function of distance to uncoupled CPW lines. Below 0mm distance, the multiconductor line is uncoupled, and composed of two CPW lines of impedance 50Ω each. They are suddenly lightly coupled (at distance 0mm), then the coupling is increased with position, until the point (at 25mm) where the coupling is abruptly adjusted to the final Josephson transmission line characteristic impedances.

S3. BAND MODELLISATION OF THE PROCESSES

In this section, we derive the equations of motion for signals traveling down the two-mode Josephson line. We then consider solutions in the form of 3 waves (pump, idler and signal) at frequencies $\omega_{P,S,I}$, the pump wave being stiff and the idler and signal wave amplitudes being slowly varying [18]. This allows us to estimate the isolation of signal waves in our device for the circulation process and the tunable coupling process.

A. Lagrangian for the two-mode Josephson line

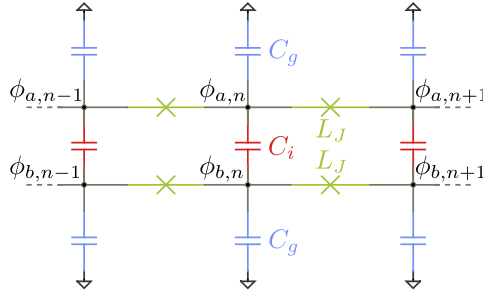


FIG. S4. **Two elementary cells of the two-mode Josephson line.** The fluxes $\phi_{a,i}$ and $\phi_{b,i}$ are defined at the nodes of the corresponding cell i .

We consider a two-mode transmission line whose elementary cells are depicted in Fig. S4. Neglecting the contribution of the first and last cell of the line, the Lagrangian of the line reads

$$\mathcal{L} = \sum_n E_J \cos\left(\frac{\phi_{a,n+1} - \phi_{a,n}}{\varphi_0}\right) + E_J \cos\left(\frac{\phi_{b,n+1} - \phi_{b,n}}{\varphi_0}\right) + \frac{C_g}{2}(\dot{\phi}_{a,n}^2 + \dot{\phi}_{b,n}^2) + \frac{C_i}{2}(\dot{\phi}_{a,n} - \dot{\phi}_{b,n})^2 \quad (\text{S3})$$

where $\varphi_0 = \hbar/(2e)$ is the reduced flux quantum. We let $\varphi_{a,n} = \phi_{a,n}/\varphi_0$, $\varphi_{b,n} = \phi_{b,n}/\varphi_0$, $L_J = \varphi_0^2/E_J$, $\omega_g = 1/\sqrt{L_J C_g}$ and $\mu = 1 + 2C_i/C_g$ and express this Lagrangian as a function of the symmetric and antisymmetric coordinates $\varphi_{\Sigma,n} =$

$(\varphi_{a,n} + \varphi_{b,n})/2$ and $\varphi_{\Delta,n} = (\varphi_{a,n} - \varphi_{b,n})/2$ as

$$L = \frac{\varphi_0^2}{LJ} \sum_n 2 \cos(\varphi_{\Sigma,n+1} - \varphi_{\Sigma,n}) \cos(\varphi_{\Delta,n+1} - \varphi_{\Delta,n}) + \frac{1}{\omega_g^2} \dot{\varphi}_{\Sigma,n}^2 + \frac{\mu}{\omega_g^2} \dot{\varphi}_{\Delta,n}^2 \quad (\text{S4})$$

The Euler-Lagrange equations then read

$$\begin{aligned} \frac{1}{\omega_g^2} \ddot{\varphi}_{n,\Sigma} &= \sin(\varphi_{\Sigma,n+1} - \varphi_{\Sigma,n}) \cos(\varphi_{\Delta,n+1} - \varphi_{\Delta,n}) - \sin(\varphi_{\Sigma,n} - \varphi_{\Sigma,n-1}) \cos(\varphi_{\Delta,n} - \varphi_{\Delta,n-1}) \\ \frac{\mu}{\omega_g^2} \ddot{\varphi}_{n,\Delta} &= \sin(\varphi_{\Delta,n+1} - \varphi_{\Delta,n}) \cos(\varphi_{\Sigma,n+1} - \varphi_{\Sigma,n}) - \sin(\varphi_{\Delta,n} - \varphi_{\Delta,n-1}) \cos(\varphi_{\Sigma,n} - \varphi_{\Sigma,n-1}) \end{aligned} \quad (\text{S5})$$

Assuming that the length a of the unit cell is much shorter than all wavelengths involved, we consider the continuous limit of these equations of motion

$$\begin{aligned} \frac{1}{\omega_g^2} \ddot{\varphi}_{\Sigma} &= a \left(\sin(a\varphi'_{\Sigma}) \cos(a\varphi'_{\Delta}) \right)' \\ \frac{\mu}{\omega_g^2} \ddot{\varphi}_{\Delta} &= a \left(\sin(a\varphi'_{\Delta}) \cos(a\varphi'_{\Sigma}) \right)' \end{aligned} \quad (\text{S6})$$

where we used the convention that $\dot{}$ designates a partial derivative with respect to time and \prime a partial derivative with respect to position.

B. Simplified sideband model

When the line is driven along φ_{Δ} with a pump at ω_P with amplitude $\epsilon_P \ll 1$ and along φ_{Σ} with a weak signal at ω_S with amplitude $\epsilon_S \ll \epsilon_P$, we have $a\varphi'_{\Sigma} \ll a\varphi'_{\Delta}$, as well as $a\varphi''_{\Sigma} \ll a\varphi''_{\Delta}$. Again, assuming the length a is much shorter than all wavelengths involved we expand to second order in $a\varphi'_{\Delta}$ and $a^2\varphi''_{\Delta}$ and to first order in $a\varphi'_{\Sigma}$ and $a^2\varphi''_{\Sigma}$ in Eq. (S6). We thus get

$$\begin{aligned} \frac{1}{\omega_g^2} \ddot{\varphi}_{\Sigma} &= a^2 \varphi''_{\Sigma} - \frac{a^4}{2} \varphi''_{\Sigma} \varphi_{\Delta}^{\prime 2} - a^4 \varphi'_{\Sigma} \varphi'_{\Delta} \varphi''_{\Delta} \\ \frac{\mu}{\omega_g^2} \ddot{\varphi}_{\Delta} &= a^2 \varphi''_{\Delta} \end{aligned} \quad (\text{S7})$$

The second equation becomes linear so that the pump propagating along φ_{Δ} is stiff and reads

$$\varphi_{\Delta}(x, t) = \epsilon_P e^{i(\omega_P t - k_P x)} + c.c. \quad (\text{S8})$$

where $k_P = -\omega_P/v_{\Delta}$ and $v_{\Delta} = a\omega_g/\sqrt{\mu}$ for a backward propagating pump (here we consider the ideal case where the pump is applied from the right sample port and that there is no impedance mismatch in the line causing reflections). Thus, by truncating the Taylor series of $a\varphi'_{\Sigma}$, $a^2\varphi''_{\Sigma}$, $a\varphi'_{\Delta}$ and $a^2\varphi''_{\Delta}$, we have neglected auto-modulation of the pump and cross-modulation from the signal. This solution can then be injected in the first equation where it modulates the properties of the Σ mode via four-wave mixing processes involving two pump photons.

Following the general method laid out in [18], we look for solutions of the equation of motion for φ_{Σ} under the form of a combination of sideband signals at $\omega_S + 2k\omega_P$ with k integer. When ω_S is close to $\omega_P(\frac{v_{\Sigma}}{v_{\Delta}} - 1)$ as prescribed in Eq. (3) the dominant sideband is at $\omega_I = \omega_S + 2\omega_P$ ($k = -1$), and we refer to it as the idler—all other processes, and in particular the one yielding a signal at $\omega_I = \omega_S - 2\omega_P$ are not phase-matched in our approach. We now focus on a simple model in which all other sideband signals are neglected. We thus look for a solution of the equation of motion under the form

$$\varphi_{\Sigma}(x, t) = \epsilon_S(x) e^{i(\omega_S t - k_S x)} + \epsilon_I(x) e^{i(\omega_I t - k_I x)} + c.c. \quad (\text{S9})$$

where $k_S = \omega_S/v_{\Sigma}$ and $k_I = -\omega_I/v_{\Sigma}$ with $v_{\Sigma} = a\omega_g$ for a forward propagating signal and backward propagating idler, and $\epsilon_S(x)$ and $\epsilon_I(x)$ are slowly varying functions ($\epsilon'_{S,I} \ll |k_{S,I}| \epsilon_{S,I}$) that we want to solve for.

One may also generalize this treatment to include all the sidebands and their mutual coupling in a matrix formalism, as developed in [37]. Applying this method to our sample parameters reveals low sidebands generation, justifying the accuracy of a simple two band model (see Fig. S5).

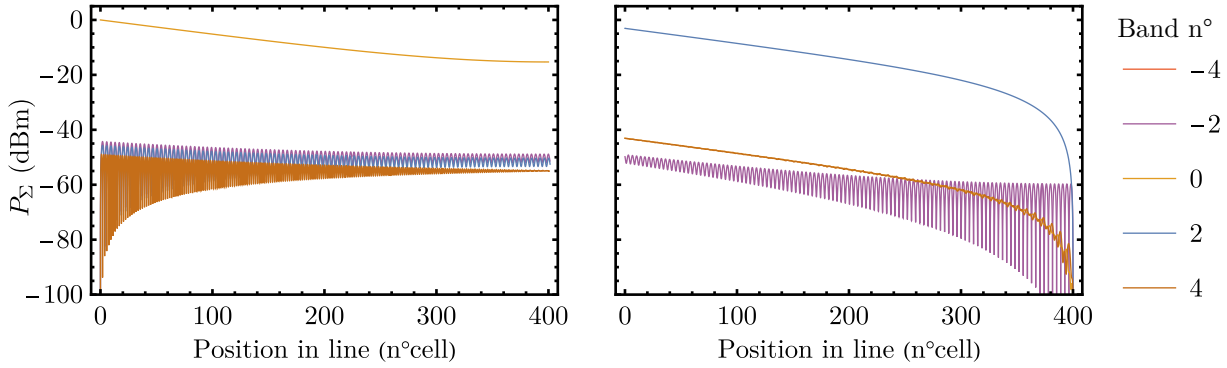


FIG. S5. **Power in sidebands** as a function of position in the two-mode Josephson line, using the matrix formalism of [37]. Band 0 corresponds to the signal band, and band 2 to the idler one. The other sidebands are 40 dB weaker than the two main bands. The simulation is ran with the sample parameters, as well as $\omega_P/2\pi = 3$ GHz, the frequency of the band 0 (or S) $\omega_S/2\pi = 6.2$ GHz and $\epsilon_P a k_P = 0.1\Phi_0$.

1. Circulator isolation

We first consider the case of a signal applied at the center frequency of the circulator working bandwidth. As a reminder, in this process a forward propagating signal can be converted to a backward propagating idler through the interaction with two backward propagating pump photons, see Fig. S6. The center frequency of the circulator is determined from the phase-matching

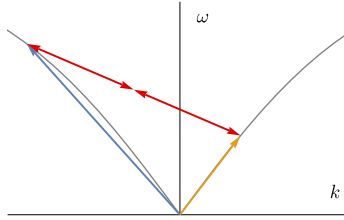


FIG. S6. **Phase-matching diagram of the circulation process.** A forward propagating signal (orange) can be converted to a backward propagating idler (blue) through the interaction with two backward propagating pump photons (red).

relations $\omega_S = \omega_I - 2\omega_P$ and $k_S + 2k_P = k_I$, yielding $\omega_S = \omega_P(\frac{v_S}{v_\Delta} - 1)$. Letting $\theta_Z = \omega_Z t - k_Z x$ for $Z = S, I, P$, we recast the first line in the equation of motion (S7) as

$$\begin{aligned}
 0 = \sum_{Z=S,I} \left(\begin{array}{l} \left(\frac{\omega_Z^2}{\omega_g^2} - a^2 k_Z^2 \right) \epsilon_Z e^{i\theta_Z} \\ + \frac{a^4}{2} (k_Z^2 \varphi_\Delta'^2 + 2ik_Z \varphi_\Delta' \varphi_\Delta'') \epsilon_Z e^{i\theta_Z} \\ + a^2 (-2ik_Z + a^2 ik_Z \varphi_\Delta'^2 - a^2 \varphi_\Delta' \varphi_\Delta'') \epsilon_Z' e^{i\theta_Z} \\ + a^2 \left(1 - \frac{a^2}{2} \varphi_\Delta'^2 \right) \epsilon_Z'' e^{i\theta_Z} \end{array} \right. \\
 \left. + c.c. \right)
 \end{aligned} \tag{S10}$$

In this expression,

- The terms of the first line sum up to zero.
- Using that $|\epsilon_Z''| \ll |k_Z \epsilon_Z'|$ (slowly varying function), we can neglect terms on the fourth line compared to terms on the third line.
- Using that $a^2 |\varphi_\Delta'^2| = a^2 |k_P^2 \epsilon_P^2| \ll 1$ and $a^2 |\varphi_\Delta' \varphi_\Delta''| = a^2 |k_P^3 \epsilon_P^2| \sim a^2 |k_P^2 k_Z \epsilon_P^2| \ll k_Z$, we can neglect the center and rightmost terms in the third line.

Altogether, we are left with

$$\sum_{Z=S,I} 2ik_Z \epsilon'_Z e^{i\theta_Z} + c.c. = \sum_{Z=S,I} \frac{a^2}{2} (k_Z^2 \varphi'_\Delta{}^2 + 2ik_Z \varphi'_\Delta \varphi''_\Delta) \epsilon_Z e^{i\theta_Z} + c.c. \quad (\text{S11})$$

Expressing $\varphi'_\Delta = -ik_P \epsilon_P e^{i\theta_P} + c.c$ and $\varphi''_\Delta = -k_P^2 \epsilon_P e^{i\theta_P} + c.c$ and given that $\theta_S + 2\theta_P = \theta_I$, we can then identify resonant terms of the form $Ae^{i\theta_S} = Be^{i\theta_I - 2\theta_P}$ and $Ce^{i\theta_I} = De^{i\theta_S + 2\theta_P}$ (and their complex conjugate) as contributing dominantly to the dynamics. We thus get two coupled differential equations for ϵ_S and ϵ_I :

$$\begin{aligned} 2ik_S \epsilon'_S &= \frac{a^2}{2} (-k_I^2 k_P^2 + 2k_I k_P^3) \epsilon_P^* \epsilon_I \\ 2ik_I \epsilon'_I &= \frac{a^2}{2} (-k_S^2 k_P^2 - 2k_S k_P^3) \epsilon_P^2 \epsilon_S \end{aligned} \quad (\text{S12})$$

and this system boils down to

$$\begin{aligned} \epsilon'_S &= i \frac{a^2}{4} \epsilon_P^* k_P^2 k_I \epsilon_I \\ \epsilon'_I &= i \frac{a^2}{4} \epsilon_P^2 k_P^2 k_S \epsilon_S \end{aligned} \quad (\text{S13})$$

One may trivially decouple this system into two separated second order differential equations. Given that $k_I k_S < 0$ in our approach, the solutions are combinations of increasing and decreasing exponential functions. In the infinite line case, since the total number of excitations in the idler and signal is preserved by the conversion process, increasing exponentials are unphysical and the solutions read $\epsilon_S(x) = \epsilon_S(0)e^{-\alpha x}$ and $\epsilon_I(x) = \epsilon_I(0)e^{-\alpha x}$ where the attenuation constant is $\alpha = \frac{a^2}{4} k_P^2 \sqrt{-k_I k_S} |\epsilon_P|^2$. Alternatively, we can solve analytically these equations with the boundary conditions $\epsilon_S(0) = \epsilon_{S,0}$ and $\epsilon_I(L) = 0$, where $L = N_{cell}a$ is the length of the device. We find:

$$\epsilon_S(x) = \epsilon_{S,0} \frac{e^{-\alpha x} + e^{-\alpha(2L-x)}}{1 + e^{-2\alpha L}} \quad (\text{S14})$$

$$\epsilon_I(x) = \epsilon_{S,0} \sqrt{\frac{k_S}{k_I}} \frac{e^{-\alpha x} - e^{-\alpha(2L-x)}}{1 + e^{-2\alpha L}} \quad (\text{S15})$$

In particular, at the end of the device, we find the total attenuation:

$$\frac{\epsilon_S(L)}{\epsilon_{S,0}} = \frac{2e^{-\alpha L}}{1 + e^{-2\alpha L}} \quad (\text{S16})$$

This is the formula used for the fits of section III, Fig. 4a.

2. Detuned isolation for the circulation process

To find the isolation bandwidth of our device, we consider the case where the signal frequency is slightly detuned from the optimal working point $\omega_S = \omega_P(\frac{v_\Sigma}{v_\Delta} - 1) + \delta$ with $\delta \ll \omega_{S,I,P}$. We still consider an idler band at $\omega_I = \omega_S + 2\omega_P$ (enforced by energy conservation), but the conversion process is imperfectly phase-matched with $k_S + 2k_P - k_I = \kappa$ with $\kappa = 2\delta/v_\Sigma$. We can still identify quasi-resonant processes from Eq. (S11) and find the coupled differential equations for ϵ_S and ϵ_I to be

$$\begin{aligned} \epsilon'_S &= i \frac{a^2}{4} e^{-i\kappa x} \epsilon_P^* k_P^2 k_I \epsilon_I \\ \epsilon'_I &= i \frac{a^2}{4} e^{i\kappa x} \epsilon_P^2 k_P^2 k_S \epsilon_S \end{aligned} \quad (\text{S17})$$

This system may be decoupled as second order equations, the equation for ϵ_S reading

$$\epsilon''_S - i\kappa \epsilon'_S - \alpha^2 \epsilon_S = 0 \quad (\text{S18})$$

This equation admits propagating solutions if $\kappa^2 - 4\alpha^2 > 0$. We thus find the isolation bandwidth limit to be set by $\kappa = 2\alpha$ and we estimate a total bandwidth $B = \frac{a^2}{2} k_P^2 |\epsilon_P|^2 \sqrt{\omega_I \omega_S}$. For our device parameters, $\omega_P = 4.63$ GHz and

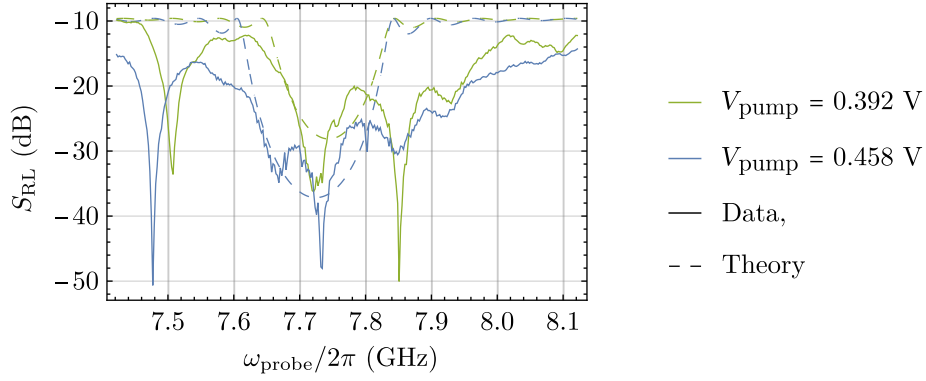


FIG. S7. **Frequency response of the device for the circulating process.** The theoretical response (dashed lines) is calculated from the fitted amplitude of section III. The process gap in the data (plain lines) is wider than the expected theoretical response. However, the shift in frequency due to the Σ mode inductance renormalization by pump amplitude (green and blue curves) is captured by the theoretical formula.

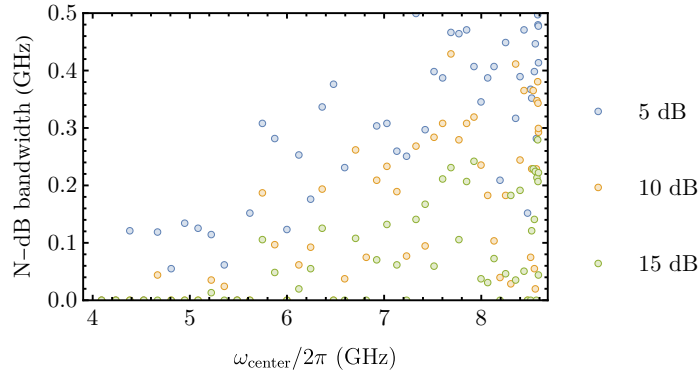


FIG. S8. **Bandwidth of the circulating process as a function of center gap frequency,** for a set a isolation levels. For each pump frequency, we locate the two points framing the $|S_{RL}/S_{LR}|$ gap at the N-dB level (N being 5, 10 or 15). The distance between these two points is the N-dB level bandwidth.

at $k_P \epsilon_P = 2\pi \Phi_{J,\max} = 2\pi 0.1$ (see following section), we get $B \sim 400$ MHz at $\omega_S = 7.8$ GHz.

Alternatively, the coupled equations (S17) may be solved analytically. The resulting expression is long, hence we only plot it—using the dispersion relations described in the next section—along with the corresponding device data (Fig S7). This formula (dashed lines) has lower bandwidth than the previous estimation and only qualitatively agrees with the data (plain lines), which shows a wider gap and additional peaks. At this point the source of this discrepancy is unknown, however the magnitude of the bandwidth is still comparable. However, we observe both the data and theoretical gap shift towards lower frequencies with increasing pump amplitude. This is due to the renormalization of the Σ mode inductance by the pump amplitude, which stems from the DC contribution of the φ_{Δ}^2 terms in (S7).

To quantify the measured bandwidth despite this disagreement, we extract a value for a set of isolation levels. For each gap center frequency, corresponding to a pump frequency, we find the frequency range for which the non-reciprocity $-20 \log |S_{RL}/S_{LR}|$ is larger than the set level, see Fig. S8. The 15-dB level is typically reached over 100 MHz for center gap frequencies above 6 GHz. Smaller levels are reached over larger widths.

3. Coupler isolation

We proceed in a similar fashion for a signal applied at the center frequency of the coupler working bandwidth. As a reminder, in this reciprocal process, a photon in the Σ mode interacts with a photon of either the backward or forward propagating pump, leading to the reflection of both photons, see Fig. S9. Considering a forward propagating photon in the Σ mode, close to $\omega_S = \omega_P \frac{v_{\Sigma}}{v_{\Delta}}$, the dominant sideband is a counterpropagating wave at $\omega_I = \omega_S$. We still use φ_{Σ} form of eq (S9), with the new

values for the idler wave. We now have to consider two counter-propagating pumps:

$$\varphi_{\Delta}(x, t) = \epsilon_{P,\text{fw}} e^{i(\omega_P t - k_{P,\text{fw}} x)} + \epsilon_{P,\text{bw}} e^{i(\omega_P t - k_{P,\text{bw}} x)} + c.c \quad (\text{S19})$$

where $k_{P,\text{fw}} = \omega_P/v_{\Delta} = -k_P$ and $k_{P,\text{bw}} = -\omega_P/v_{\Delta} = k_P$. In that case, we have $k_S + k_{P,\text{bw}} = k_I + k_{P,\text{fw}}$. Eq (S11) is still valid, and after identifying the dominant resonant terms, we get two coupled differential equations:

$$\begin{aligned} 2ik_S \epsilon'_S &= \frac{a^2}{2} (-2k_I^2 k_P^2 + 4k_I k_P^3) \epsilon_{P,\text{fw}} \epsilon_{P,\text{bw}}^* \epsilon_I \\ 2ik_I \epsilon'_I &= \frac{a^2}{2} (-2k_S^2 k_P^2 - 4k_S k_P^3) \epsilon_{P,\text{bw}} \epsilon_{P,\text{fw}}^* \epsilon_S \end{aligned} \quad (\text{S20})$$

which are very similar to coupled equations (S12), up to a change $\epsilon_P^2 \rightarrow 2\epsilon_{P,\text{bw}} \epsilon_{P,\text{fw}}^*$. The factor 2 stems from the symmetry of the product terms φ_{Δ} in (S11) and can be understood as an alternative path in the phase matching diagram, as shown in Fig S9.

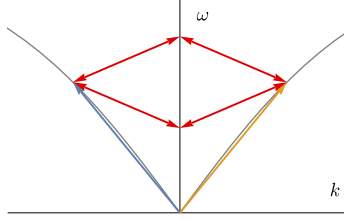


FIG. S9. **Phase matching paths of the tunable coupling process.** The signal (orange) and idler (blue) arrows can be arranged in a closed form through the top two pump arrows (red), or the bottom two. This is equivalent to the two possible orders of terms of φ_{Δ} in (S11).

The coupled equations are solved in the same manner as the circulating process case, and used for the fitting procedure of the tunable coupling process in section III.

C. Lumped element corrections

1. Lumped phase-matching relation

The non-linear transmission line is made of discrete lumped elements. When the wavelength of the traveling wave is much larger than the elements, then the speed of the wave is roughly constant and given by the equations (5). However, as frequency is increased the wavelength shrinks to become comparable with the size of the elements. This translates into a slowdown of the wave, and the apparition of a cut-off frequency above which waves cannot propagate. The cut-off frequency and dispersion relation are further renormalized by the plasma frequency of the junctions (modeled by a capacitance C_J in parallel with each Josephson junction). We then have to replace the simple speed by a more complete relation [60]:

$$\begin{aligned} k_{\Sigma}(\omega) &= \frac{1}{a} \arccos \left(1 + \frac{C_g L_{J,\Sigma} \omega^2}{-2 + 2C_J L_{J,\Sigma} \omega^2} \right) \\ k_{\Delta}(\omega) &= \frac{1}{a} \arccos \left(1 + \frac{(C_g + 2C_i) L_J \omega^2}{-2 + 2C_J L_J \omega^2} \right) \end{aligned} \quad (\text{S21})$$

The dispersion relation for the Σ mode, computed using the fitted value for the circuit parameters, is plotted in Fig S10. The cut-off frequency for the Σ mode is given by:

$$\omega_{co} = \frac{2}{\sqrt{L_{J,\Sigma}(C_g + 4C_J)}} \quad (\text{S22})$$

Using the non-linear dispersion relations (S21), we no longer obtain closed form expressions for the frequencies of the dips associated to the various processes. However, we can still express the phase-matching conditions as transcendental equations. As an example, we establish the equation for the signal to idler conversion of the isolation process, starting from the energy (1) and impulsions (2) conversion, we get:

$$k_{\Sigma}(\omega_i) = -k_{\Sigma}(\omega_i) + 2k_{\Delta}(\omega_p)$$

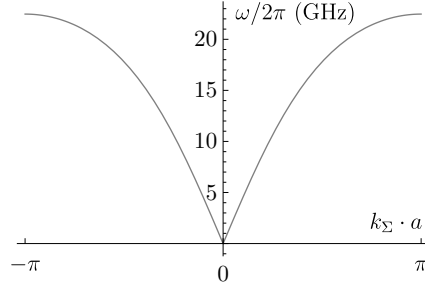


FIG. S10. **Dispersion relation of the sample Σ mode.** At low frequencies, the simplified formula for phase velocity ω/k of equation (5) applies. When the frequency becomes comparable with the cut-off of the line, the phase velocity diminishes. The cut-off frequency corresponds to a phase $\pm\pi$ across a cell, or equivalently half a wavelength.

which, along with the lumped element dispersion relation, gives the following transcendental equation:

$$\begin{aligned}
 -\arccos\left(1 + \frac{C_g L_{J,\Sigma} (\omega_s + 2\omega_p)^2}{-2 + 2C_J L_{J,\Sigma} (\omega_s + 2\omega_p)^2}\right) \\
 = \arccos\left(1 + \frac{C_g L_{J,\Sigma} \omega_s^2}{-2 + 2C_J L_{J,\Sigma} \omega_s^2}\right) - 2 \arccos\left(1 + \frac{(C_g + 2C_i) L_J \omega_p^2}{-2 + 2C_J L_J \omega_p^2}\right) \quad (\text{S23})
 \end{aligned}$$

We then numerically plot the solutions to this equations, as well as the corresponding ones for the tunable coupling and aliased circulation processes, and manually fit the gap lines on the colormaps of Fig 3. The fit parameters are the products $L_J C_g$, $L_J(C_g + 2C_i)$ and the junction plasma frequency f_{plasma} , and can be found in Table I. Note that in our analysis, we have computed dispersion relations neglecting the Josephson junctions nonlinearity (considering junctions as linear inductances L_J). Accounting for the cosine inductive potential of the junctions leads to a renormalization of the wave phase velocity of the Σ mode as the pump amplitude increases (the signal and idler wave amplitudes are small enough that their impact can be safely neglected). The fitted curves on Fig 3 use this correction for a value of $\Phi_{JJ} = 0.1\Phi_0$ consistent with the calibration of the pump amplitude performed in the following section. Its effect is captured in the renormalization factor $L_{J,\Sigma}/L_J$ described in the table I.

Parameters	Fit	Design
$v_{\Sigma,0} = 1/\sqrt{L_J C_g}$ (cell/ns)	94.1	90.4
$v_{\Delta,0} = 1/\sqrt{L_J (C_g + 2C_i)}$ (cell/ns)	29.8	28.9
f_{plasma} (GHz)	38.0	/
$L_{J,\Sigma}/L_J$	1.11	/

TABLE I. Fit and design parameters of the device.

Note that these parameters are linked to the speed of the waves, while the parameters L_J , C_g and C_i do not appear isolated in the transcendental equations. To extract the individual parameters, an additional measurement is required. Impedance measurement would be ideal, as $Z_\Sigma = \sqrt{\frac{L_J}{C_g}}$. It is accessible through time domain reflectometry. However, in our case this proves to be too unprecise for quantitative estimation, as developed in supplemental section S4.

2. Phase across a junction

In the limit of pump Δ amplitude dominating the signal Σ amplitude, we evaluate the phase across a single Josephson junction of the line ϕ_{JJ} :

$$\begin{aligned}
 \Phi_{JJ,n} &= \Phi_{a,n+1} - \Phi_{a,n} \\
 &= \varphi_0 (\varphi_{\Delta,n+1} - \varphi_{\Delta,n})
 \end{aligned}$$

where we used the mode definition of section S3 A. We now use the continuous limit approximation, and the lumped element correction will stem from the use of the dispersion relation of the Δ mode (S21):

$$\Phi_{JJ}(x) = a\varphi_0\varphi'_\Delta$$

where we dropped the n suffix. With the ansatz (S8), we find:

$$\Phi_{JJ}(x) = ia\varphi_0 k_P \epsilon_P e^{i(\omega_p t - k_P x)} + c.c$$

along with $k_P = k_\Delta(\omega_p)$ and the value of ϵ_P extracted from the theoretical fit of Fig 3, we obtain the sought amplitude:

$$\Phi_{JJ} = 2ia\varphi_0 k_\Delta(\omega_p) \epsilon_P \quad (\text{S24})$$

D. Attenuation fits

With the equation (S16) we can extract, from the measured attenuation, the pump amplitude ϵ_P , which we convert to Φ_{JJ} with equation (S24). Finally, we compute the ratio between the phase Φ_{JJ} and the applied pump voltage at room temperature $r_{\leftarrow} = \Phi_{JJ\leftarrow}/V_{\text{pump}}$ (see Fig. S11). In principle, we should only get a backward propagating pump. However, we measure non-zero backward attenuation, which we interpret as resulting from a reflection of the pump inside the two-mode Josephson line. We can use the backward attenuation data and the same previous steps to estimate the amplitude $\Phi_{JJ\rightarrow}$ of the spurious forward propagating pump. We compute the ratio $r_{\rightarrow} = \Phi_{JJ\rightarrow}/V_{\text{pump}}$.

The tunable coupling process, which leads to the apparition of a dip at a different probe frequency (see Sec. S3 B 3) depends on the product of forward and backward propagating amplitudes, which have been fitted as detailed above. As a supplementary check, we use the previously fitted backward ratio r_{\leftarrow} and fit the tunable coupling attenuation data with another forward ratio $r_{\rightarrow, \text{Co}}$. This new forward ratio is slightly mismatched with the previous ratio r_{\rightarrow} . This may be explained by the crude modeling involving constant amplitudes for pump waves propagating forward and backward throughout the line, whereas additional measurements indicate that a significant reflection occurs near the middle of the line (see Sec. S4). This also explains why compensation does not work well. We re-run the same procedure after adjusting the phase and amplitude of a tone applied from the other port of the sample to optimize performances (see Sec. S5). We see only a modest improvement on the ratio of backward to forward amplitudes $r_{\leftarrow}/r_{\rightarrow}$.

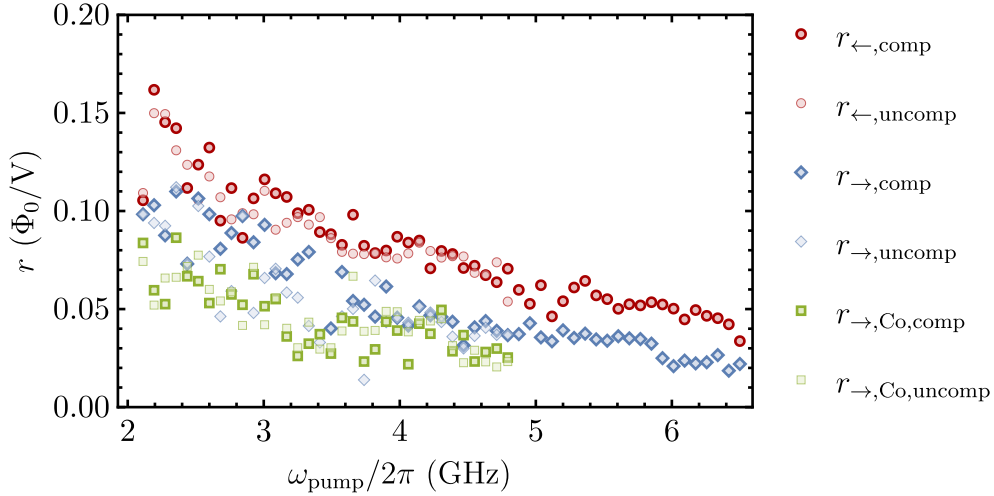


FIG. S11. **Fit parameters of the attenuation** $r = \Phi_{JJ}/V_{\text{pump}}$, ratio between the pup amplitude at room temperature (expressed in volts over a 50Ω line) and the wave amplitude inside the two-mode Josephson line (expressed as phase amplitude across a junction). **Left**, desired backward propagating pump ratios in the compensated (dark red) and uncompensated cases (light red). The ratio is slightly higher in the compensated case, showing its modest beneficial effect. **Right**, ratio for the spurious forward propagating pump obtained from spurious circulating process in compensated and uncompensated cases (dark blue and light blue, respectively), as well as from the tunable coupling process (dark green and light green). There is little difference between the two cases. However the coupling process values are only slightly mismatched with the spurious circulating one.

S4. TIME DOMAIN MEASUREMENT

In order to estimate the level of reflection within the sample, and confirm the hypothesis that the pump is primarily reflected within the non linear transmission line (and not to the connecting circuitry), we perform time domain reflectometry

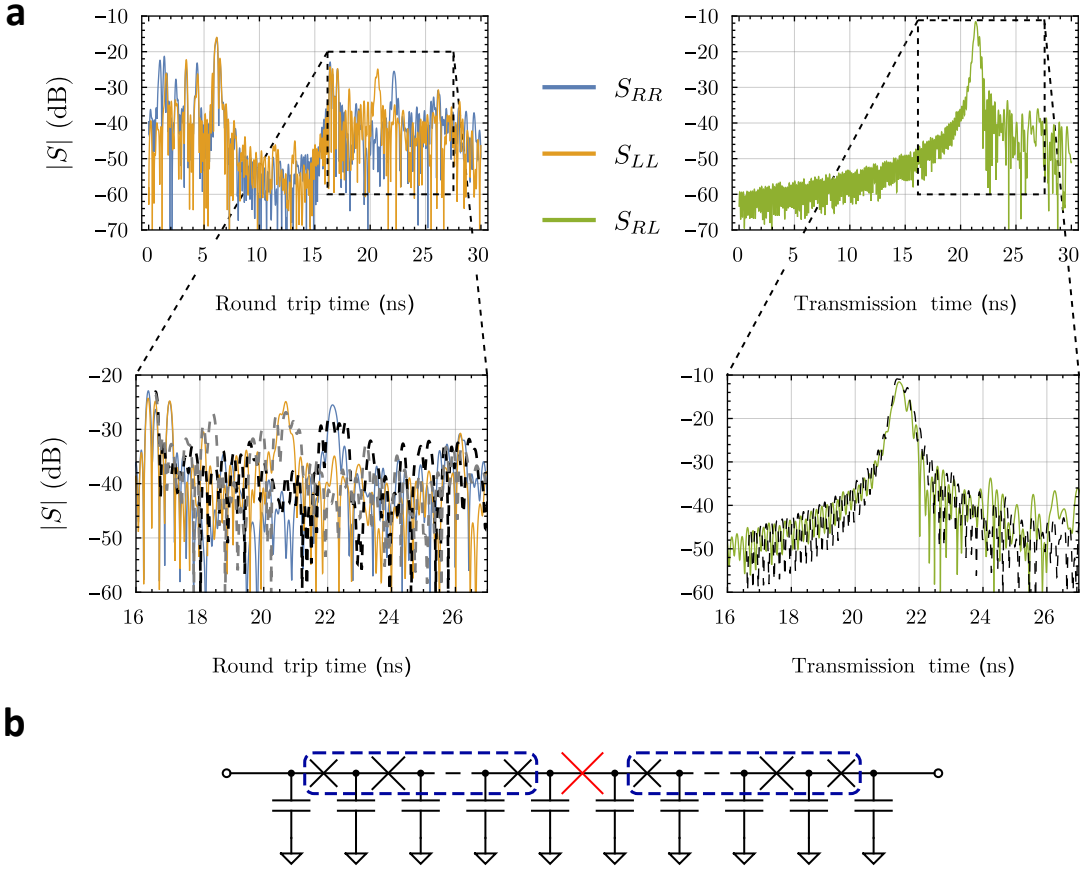


FIG. S12. **Time domain measurements.** **a:** full range of time domain impulse response measurements in reflection and transmission. We identify the portion of the time domain that corresponds to the lumped transmission line. The dip in reflection during the transmission in the 1m cable connected just before the sample is a good indicator of the relevant portion. **Dashed square boxes:** magnified time domain measurements in the two-mode Josephson line. The dashed lines are the time domain impulse response of the simple model presented in S12b. There is qualitative agreement with the data, in particular reproducing the two reflection peaks that are at a different position depending on the input direction. Exact agreement is not possible as the model is randomized, and sensitive to the specific realization of disorder. In the right panel picturing the time response in transmission, we notice the main peak is wider than the resolution of 200 ps. This is consistent with the dispersion caused by the plasma frequency of the junctions, which is included in our model. **b:** Simple one-mode model used to reproduce the time domain impulse response of the sample. The red junction represents a highly out of spec defect. The blue dashed rectangles indicate that disorder is applied to the other junction, modeling the fabrication parameters spread. To model disorder, we sample the Josephson junction inductances uniformly in an interval $[0.97 L_J, 1.03 L_J]$ centered at the nominal design value, and the defect inductance is 1.5 times the nominal value.

measurements.

Traditionally, time domain measurement is performed by launching a short pulse or a stepwise excitation pulse towards the device under test, and monitoring as a function of time the reflected and transmitted signals. However, this is impractical and noise-prone in complex radio-frequency systems [61] such as our device in the cryostat. Fortunately, the time domain measurement is virtually equivalent to a frequency domain one, up to a Fourier transform [61]. In addition, frequency domain measurement benefits of the increased precision from the calibration. The analyzed portion of the system, and consequently the complexity of interpretation of the reflection pattern, is greatly reduced thanks to the shift of the reflection planes closer to the sample obtained using calibration standards (see section S1). Despite all the benefits, there still are limitations. Because of the circulators, the device can only be measured in a limited band, excluding DC and low-frequencies. This has the double inconvenient of reduced resolution (as low-pass data including DC could have been mirrored to negative frequencies, doubling resolution) and the inability to reconstruct the response of a system to a step input (which necessitates DC response). Only an impulse response can be computed, for which the magnitude of the reflected and transmitted peaks is less reliable than the magnitude of the step response. Each successive reflection before the impulse reaches the two-mode Josephson line in the calibrated data adds uncertainty. Indeed the power reaching a given impedance defect, and its associated reflection magnitude we detect, is affected by the previous reflections. Additionally, the complex phase of the impulse response is hardly usable,

whereas the sign of the real step response would have been easily interpreted to distinguish types of impedance mismatches. We perform the inverse Fourier transform on frequency domain S-parameters of the Σ mode, while no pump is being applied to the Δ mode, to obtain the time domain S-parameters in Fig S12. The original frequency data is sampled from 4 GHz to 10 GHz, that is a 6 GHz bandwidth. With minimal windowing applied, this results in a resolution of about 200 ps ($1.2/\text{BW}$, [61]). In a typical coaxial cable in which waves propagate at $0.7c$, the resolution is about $6 \cdot 10^{-2}$ m. However, in the non-linear device, speed (v) is 93.8 cell/ns, yielding a resolution of 18.8 cells, enough to approximately locate a defect within the line. The results of this effective time domain measurement is presented in Fig. S12, and exhibits multiple reflection peaks separated by periods where the reflected signal is negligible. We interpret the long dip in reflection as the 1 m cable connected to the sample (expected 9.5 ns for the round-way trip), and identify the following portion as the device itself (only the lumped element line part is resolvable given the greatly reduced speed inside it). In dashed square boxes in Fig S12, the relevant portion is magnified. Two reflection peaks are noticeable close to the middle of the transmission line. This corresponds to internal spurious reflections. The reflection peaks for the two impulse input port do not overlap as the defect is not perfectly centered in the line. We reproduce qualitatively the reflection response using a simple one mode model, shown in Fig S12b, where a single out of spec junction, with an inductance 1.5 times the nominal value, is responsible for most of the reflection. To model disorder, we sample the Josephson junction inductances uniformly in an interval $[0.97 L_J, 1.03 L_J]$ centered at the nominal design value. This reproduces the reflection floor. With this simple one-mode model and analyzing reflection peaks when the nonlinear two-mode line connects to the tapered feedline (designed such that negligible reflections should occur if the nonlinear portion is perfectly on spec), we can estimate the impedance of the Σ propagating mode as $Z_\Sigma \approx 105\Omega$, in qualitative agreement with the design value. However, the quantitative results are not reliable because of the previously explained time-domain technique limitations as well as the simplified nature of the one mode model, which is unable to precisely reproduce the two-mode nature of the line.

S5. PUMP COMPENSATION

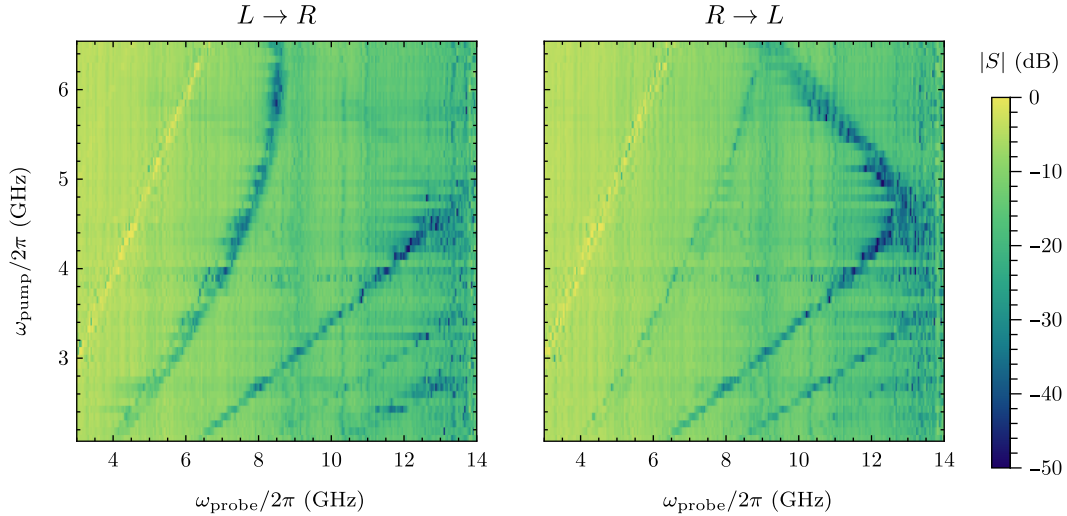


FIG. S13. **Forward and backward transmissions** of a probe applied to the Σ mode in presence of an uncompensated pump on the Δ mode, against pump and probe frequencies. The pump is sent only at the right Δ port. The gaps (visible as blue lines on the maps) are qualitatively the same as in the compensated pump case, shown in main text Fig 3.

As indicated by the unexpected non zero backward attenuation in circulation mode (see Sec. III and confirmed by time domain measurements (see Sec. S4, internal reflections within the sample result in a pump traveling in both directions inside the line, despite a pump tone being sent to a single Δ port. When acquiring the data presented in the main text figures, we send a second pump wave from the second port of the sample in order to try and cancel the spurious forward propagating wave within the sample. Note that in principle, this strategy should allow perfect cancellation of the spurious wave if reflections only occur in the feedlines or at the ports of the two-mode Josephson line. For completeness, we show in Fig S13 the same data without compensation, when a single pump tone is sent backward to a single Δ port of the sample. It is qualitatively similar to the main text figure, but the spurious gaps (leftmost blue line in the backward transmission and faint blue line in the bottom right corner in the forward transmission) are a little less noticeable, and the reciprocal coupler process is slightly more pronounced. To systematically adjust the amplitude and phase of the compensation pump wave relative to the main pump wave (at each pump frequency, we end up with only two scalar compensation parameters), we established the following procedure. We start by evaluating the quality of the isolation for a given set of main pump amplitude $A_{p,\text{main}}$ (with phase referenced at 0), compensation

pump amplitude $A_{p,\text{comp}}$, and compensation pump phase $\phi_{p,\text{comp}}$. The cost function on which we optimize the compensation parameters combines the desired forward attenuation and the undesired backward attenuation. In detail, we define two distinct cost functions for each contribution:

$$\begin{aligned} \mathcal{C}_{\text{isolation}}(A_{p,\text{main}}, A_{p,\text{comp}}, \phi_{p,\text{comp}}) &= 20 \log_{10} \overline{|S_{21}|}(A_{p,\text{main}}, A_{p,\text{comp}}, \phi_{p,\text{comp}}) \\ \mathcal{C}_{\text{reverse}}(A_{p,\text{main}}, A_{p,\text{comp}}, \phi_{p,\text{comp}}) &= -20 \log_{10} \overline{|S_{12}|}(A_{p,\text{main}}, A_{p,\text{comp}}, \phi_{p,\text{comp}}) \end{aligned}$$

where the average $\bar{\cdot}$ is taken over the range $[\omega_s - \Delta\omega, \omega_s + \Delta\omega]$ with $\Delta\omega = 300$ MHz, and encompasses the gap width. From these two averages, we define a total cost, and the total cost function reads:

$$\mathcal{C}_{\text{total}}(A_{p,\text{main}}, A_{p,\text{comp}}, \phi_{p,\text{comp}}) = \mathcal{C}_{\text{isolation}}(A_{p,\text{main}}, A_{p,\text{comp}}, \phi_{p,\text{comp}}) + 0.6\mathcal{C}_{\text{reverse}}(A_{p,\text{main}}, A_{p,\text{comp}}, \phi_{p,\text{comp}}) \quad (\text{S25})$$

We evaluate the cost for values of $A_{p,\text{main}} \in \{A_i\}_{i \in [1, N_A]}$, $A_{p,\text{comp}} \in \{A_i\}_{i \in [1, N_A]}$ and $\phi_{p,\text{comp}} \in \{\phi_i\}_{i \in [1, N_\phi]}$. To evaluate the cost as a function of a given ratio $r = A_{p,\text{comp}}/A_{p,\text{main}}$, for each value of $A_{p,\text{main}} = A_i$, we post-select the swept value $A_{p,\text{comp}} = A_{j_i}$ closest to ratio $\cdot A_i$. The global cost for a value of ratio and phase is calculated as a sum over the corresponding pump amplitudes:

$$\mathcal{C}_{\text{global}}(r, \phi_{p,\text{comp}}) = \sum_i \mathcal{C}_{\text{total}}(A_{p,\text{main}}, A_{p,\text{comp}}, \phi_{p,\text{comp}}) \quad (\text{S26})$$

We find the optimal ratio and $\phi_{p,\text{comp}}$ by sweeping both parameters and selecting the lowest global cost.

We tried a similar procedure to maximize the attenuation of the tunable coupler process but it did not yield noticeable improvements. We believe the spurious internal reflections already generate a strong forward propagating pump, which we barely intensify with our forward sent pump tone. A modest increase of the forward pump is even less noticeable than the modest decrease we achieved with the isolator process compensation.

S6. DYNAMIC RANGE

In this section, we estimate the dynamic range of the device, that is the maximum signal wave power it can handle before its performances degrade. We first need to relate the power received at the Σ input of the line to the power sent at room temperature with the VNA generating the signal wave. Indeed, with the calibration described in supplemental S1 we only know the attenuations of the line for a full round trip. This is a fundamental limitation of this type of calibration, we do not know the attenuation of the input line by itself. To calibrate the one-way attenuation, we rely on the self-Kerr modulation of the Σ mode, in the absence of any pump on the Δ mode. From the equation of propagation of the Σ mode (S6):

$$\begin{aligned} \frac{1}{\omega_g^2} \ddot{\varphi}_\Sigma &= a \left(\sin(a\varphi'_\Sigma) \right)' \\ &= a^2 \cos(a\varphi'_\Sigma) \varphi''_\Sigma \end{aligned}$$

Using the order 0 of the Jacobi-Anger expansion, and the ansatz $\varphi_\Sigma = \varphi_{\Sigma,0} e^{i(\omega t - kx)} + c.c.$, we find the following dispersion relation with self-Kerr effect:

$$\omega(k, \varphi_{\Sigma,0}) = \omega_g a k \sqrt{J_0(k \varphi_{\Sigma,0})} \quad (\text{S27})$$

where J_0 is the Bessel function of the first kind, and of order 0. From the VNA measurement, at frequency $\omega_0/2\pi$, we extract the relative phase added by self-Kerr, which is:

$$\begin{aligned} \Delta\phi &= \frac{L}{a} k(\omega_0, 0) - \frac{L}{a} k(\omega_0, \varphi_{\Sigma,0}) \\ &= \frac{L}{a} \frac{\omega_0}{\omega_g} - \frac{L}{a} k(\omega_0, \varphi_{\Sigma,0}) \end{aligned}$$

with $\frac{L}{a}$ the number of cells, and $\varphi_{\Sigma,0}$ is to be calibrated. From this relation and the measured relative phase, we get $k(\omega_0, \varphi_{\Sigma,0})$. We numerically solve $\omega(k, \varphi_{\Sigma,0}) = \omega_0$ to find the value of $\varphi_{\Sigma,0}$. We repeat this process for all measured values of ω_0 and for several signal amplitudes. We plot in Fig S14a the value of $\varphi_{\Sigma,0}$ as a function of VNA room-temperature amplitude for several values of $\omega_0/2\pi$. The estimated value of $\varphi_{\Sigma,0}$ is proportional to the RT amplitude of the signal wave, which is expected in the linear loss regime. We extract this slope for all measured values of ω_0 , as plotted in Fig S14b and find the expected attenuation

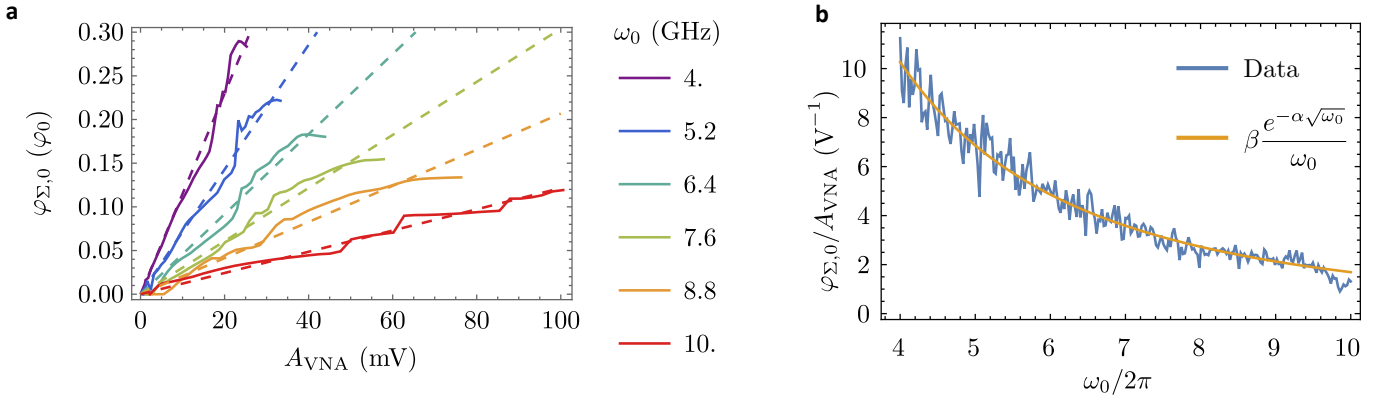


FIG. S14. **Estimation of the line attenuation.** **a**, In-line amplitude $\varphi_{\Sigma,0}$ as a function of VNA room-temperature amplitude. The two are proportional. Dashed lines fit the linear relationship. **b**, Fitted attenuation ratio as a function of VNA frequency. The data trend follows the expected dependency composed of exponential resistive losses increasing with $\sqrt{\omega_0}$, and the phase being the integral of the voltage yields the front factor $1/\omega_0$. β and α are fit parameters.

scaling in $\frac{1}{\omega_0} e^{-\alpha\sqrt{\omega_0}}$. The resistive losses increase exponentially with $\sqrt{\omega_0}$. The phase being the integral of the voltage yields the front factor $1/\omega_0$.

We have related the amplitude in the line in the Σ mode, to the amplitude sent from the VNA at room-temperature. We now measure the device isolation in circulator mode, as well as its insertion loss in the backward direction, as described in section III, while varying the VNA amplitude, expressed in terms of power inside the line (see Fig. S15).

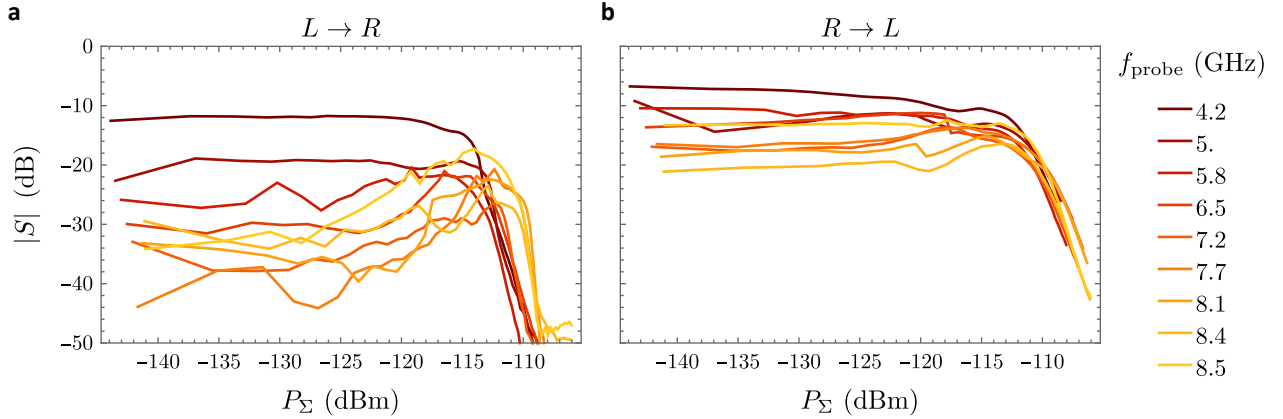


FIG. S15. **Dynamic range of the circulator process at various signal dip frequencies.** The displayed frequencies correspond to linear spacing in pump frequency. **a**, Forward signal isolation as a function of in-line power, at the center gap frequency. The isolation is fairly constant up to a probe power of -125 to -120 dBm, it degrades if the power is increased further. **b**, Backward transmission as a function of in-line power, at the center gap frequency. The transmission is fairly constant up to a probe power of -120 dBm, after which it degrades.

The isolation is stable up to a probe power of -125 to -120 dBm, depending on the probe frequency. Increasing the power further reduces it until -115 to -110 dBm. Going beyond -110 dBm the transmission in both direction collapses; this is the limit of the line. This value is acceptable for quantum level signals, but too low for already amplified signal. This is expected given the inductance L_J of the junctions, which translates to a low critical current value. A solution for this issue, at the cost of higher fabrication complexity, would be to increase the number of junctions, in order to lower the phase across a single junction. This can either be done by adding cells to the line and reducing the values of L_J and capacitances accordingly, or, by keeping the total cell value the same but putting multiple junctions in series per cell, as done for example in [23].

S7. POWER CIRCULATION, SIDEBAND GENERATION AND INTER-MODE LEAKAGE

A. Power circulation

In this section, we investigate the conversion aspect of the circulation process. To proceed, we send a continuous wave probe tone to one Σ port using the VNA as a source, and we measure the power spectrum transmitted or reflected, at an the output Σ lines (see setup details in Fig. S1). We expect the device to generate sidebands, due to unmatched spurious wave-mixing processes. In essence, sending a signal at ω_{probe} while a pump is being applied at ω_P will create bands at $\omega_{\text{probe}} + n\omega_P$, with $n \in \mathbb{Z}$. In particular, if ω_{probe} is chosen to phase match the circulator process, then the backward reflected band $n = 2$ is the corresponding idler band, and the other values of n are spurious sidebands. Note that if the activated processes are strictly four wave-mixing, there would be no sidebands at odd values of n . We still measure some of them in the following. In practice detecting a large number of sidebands is complex. Indeed, the pump frequencies are comparable to the signal frequencies, and the sidebands spread from near-DC to the cut-off of the line, over 20 GHz. We only measure sidebands that are inside the isolators and amplifiers bandwidth, which is 4 to 10 GHz. The unknown attenuation of the output lines also prevents us from directly comparing the outcoming sideband powers. We use the attenuation estimation of the input line of the previous supplemental S6, together with the calibration of round-trip attenuation described in supplemental S1 [56, 57], in order to estimate the output lines transmission magnitudes. We thus get an estimation of the power coming out of the transmission line from the power measured at room temperature, for the covered frequencies.

In Fig S16, we measure the spectra of the out-coming signals for different transmission and reflection configurations of the Σ ports, for a single pump frequency of $\omega_p/2\pi = 2.19$ GHz. We probe the system either at the signal or idler frequency (related to the pump frequency through the phase-matching condition Eq. (3)), respectively corresponding to the band 0 and band 2 as previously introduced. In all configurations the dominant contributions to the power spectra occurs at these two frequencies, as expected from wave circulation in the device. In particular, the rightmost panels show that probe waves are reflected and frequency converted as detailed in Sec. I of the paper. Nevertheless, we detect a non negligible power contribution at some other band frequencies, reported in Fig. S16. In particular, the power of band 1 is only 10 to 20dB lower than that of the main band when probing the system at ω_{signal} and applying a large pump amplitude (top panels). This is unexpected given that our device should not allow three-wave mixing.

In principle, waves circulate within the device while preserving the total number of photons. To investigate further this point, we plot in Fig S17 the isolated sent band compared to the generated corresponding band for the two processes, in photon flux in linear scale. We do not get photon flux conservation, but the order of magnitude are consistent, and few dBs of incertitude in the power estimation over the wide range of frequencies is enough to explain the discrepancy observed.

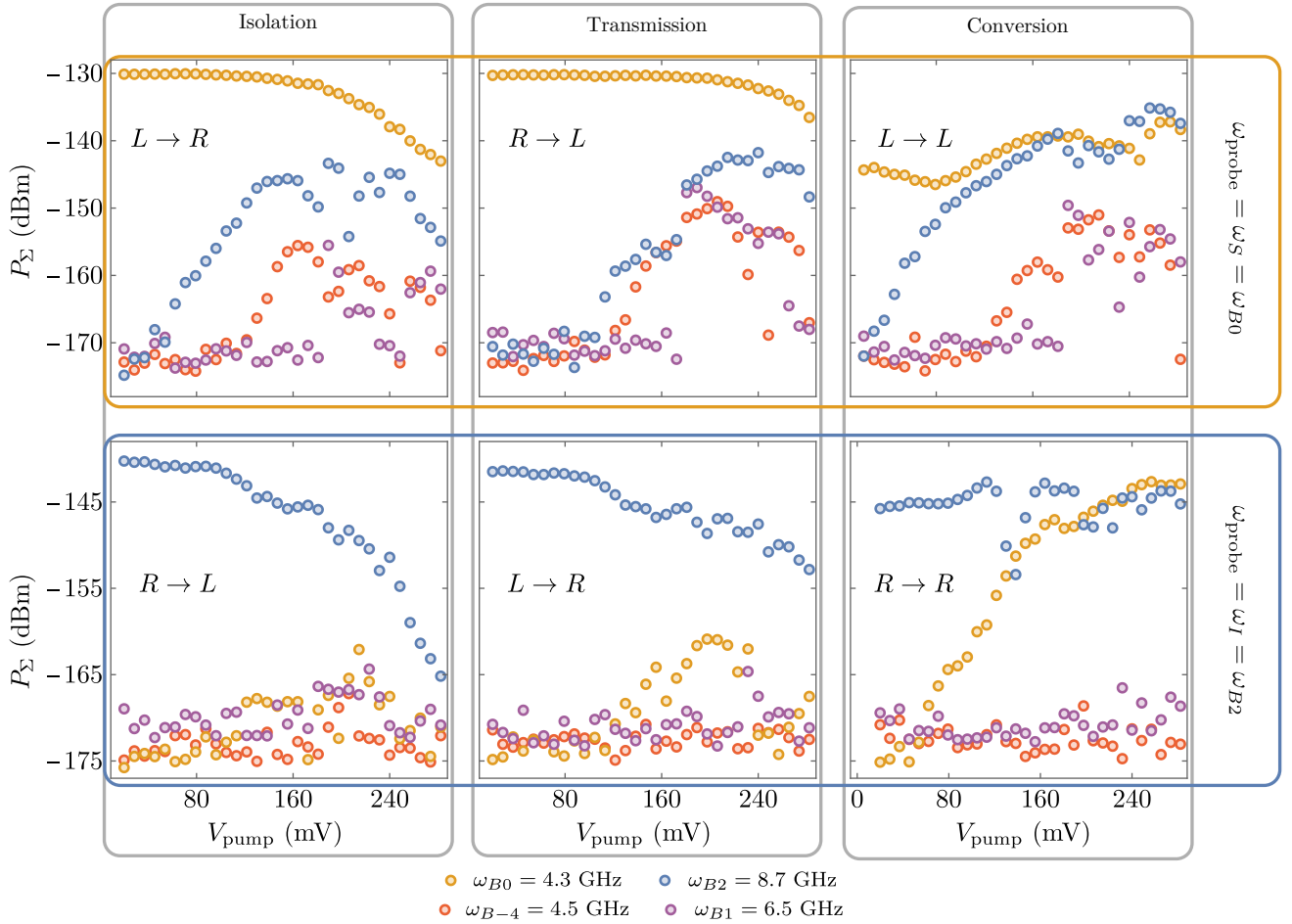


FIG. S16. **Power of sideband waves leaking out from one of the device Σ port**, in presence of a pump at $\omega_P = 2.19$ GHz, as a function of the pump amplitude. We represent the power of the only bands that lie within the working bandwidth of the circuitry, see S1. In particular, we don't have access to the most prominent sidebands in the previous simulation (see Fig. S5). Label $i \rightarrow j$ indicate that the probe wave is applied from port i and the generated sideband wave are detected on port j , where i and j can be L (left) or R (right). On top panels, the probe is adjusted at the band 0 frequency ($\omega_{\text{probe}} = \omega_S$, respecting the phase-matching condition (3)), while on bottom panels its is adjusted at the band 2 frequency ($\omega_{\text{probe}} = \omega_I$, also phase-matched). In the leftmost column, we analyze the transmitted spectrum in the direction of isolation of the circulator. As expected the transmitted probe power decreases with pump amplitude (band 0 for the top panel, band 2 for the bottom panel). The increasing power of band 2 in the top panel may be attributed to secondary reflection of the idler wave after its expected reflection and frequency conversion by the circulator. The non-zero power of other bands indicate that spurious conversion processes are active. In the middle column, we analyze the transmitted spectrum in the direction along which the circulator should not attenuate the probe wave. The decrease in transmitted probe power versus pump amplitude is attributed to internal reflections of the pump wave (see Sec. III). The non-zero power detected at other bands frequency is again attributed to spurious reflections or conversion processes. In the rightmost column, we detect the reflected field, whose spectrum should reveal frequency conversion of the probe wave. The increase of the power of band 2 versus pump amplitude in the top panel (power of band 0 for the bottom panel) confirms this conversion and the circulation of waves in the device. The large constant power in band 0 for the top panel (band 2 for the bottom panel) indicates that the probe is partly reflected without frequency conversion. We attribute these reflections to impedance mismatches in the sample or in the feedlines. As a broader comment, the optimal working amplitude at this pump frequency is around 180 mV. The non-negligible level of sidebands at this amplitude (including the $B1$ band hinting at 3 wave-mixing) indicates the model (see Sec. S3) is inaccurate, and, at least for some weaker junctions, the low-amplitude linear approximation may be invalid.

B. Pump harmonics

Using the same detection setup and estimate for the attenuation of the output lines, we now turn to characterizing the pump leakage to the Σ propagation mode. In Fig. S18, we report the detected power at the pump frequency $\omega_P/2\pi = 2.19$ GHz at multiples of this frequency, while sweeping the pump amplitude at room temperature. The highest harmonic order measurable is limited by the spectrum analyzer. We observe mainly that the 3rd harmonic scales with the fundamental while the power of the 2nd harmonic remains below our detection level. The device therefore mainly exhibits 4 wave-mixing behavior. On the right

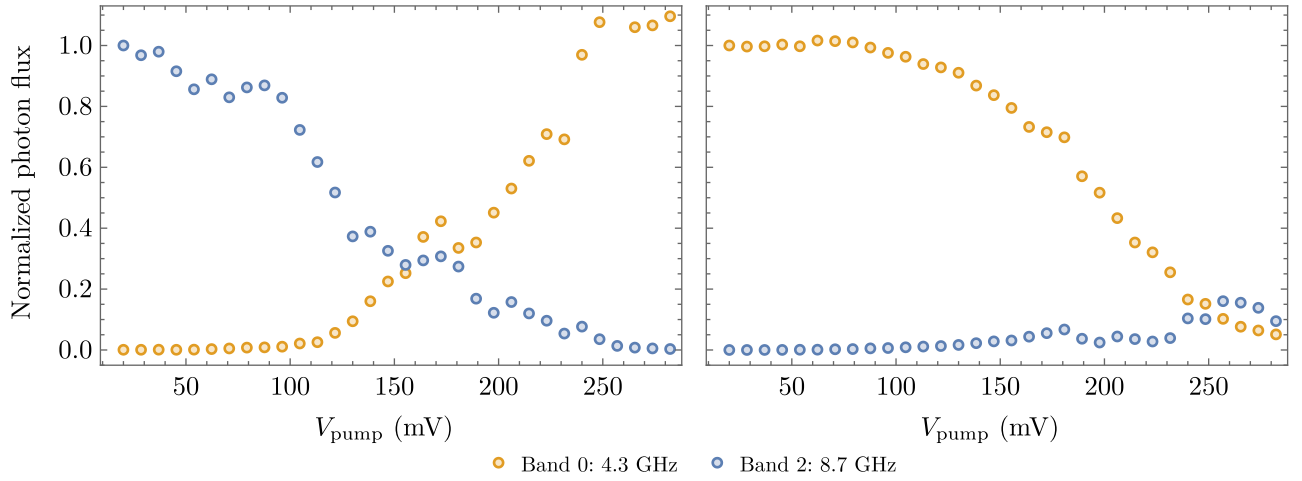


FIG. S17. **Conversion measurement by spectrum analysis.** Power level, in terms of photon flux, normalized to the input power, for the signal and idler bands as a function of the pump amplitude. The backward propagating pump, and its forward compensation tone, is set at 2.19 GHz. **Left**, Idler to signal conversion. The idler is sent at the right port. The transmitted idler, or band 2, is measured at the left port and the converted signal, or band 0, is measured at the right port. The transmitted photon flux (at ω_{idler}) decreases while the reflected photon flux (at ω_{signal}) increases. The signal photon flux going over 1 indicates that the attenuation of the feedline connecting to the port 1 is over-estimated at ω_{signal} or under-estimated at ω_{idler} . **Right**, Signal to idler conversion. The signal tone is sent at the right port. The transmitted signal, or band 0, is measured at the left port and the converted idler, or band 2, is measured at the right port. Here, we do not observe a significant increase in the normalized reflected photon flux normalized as the pump amplitude increases. This may indicate that the attenuation of the feedline connecting to the port 2 is over-estimated at ω_{signal} or under-estimated at ω_{idler} .

panel, we repeat the measurement for varying pump frequencies, while the pump amplitude is set so that the oscillating phase across a junction is $\Phi_{\text{JJ,max}} = 0.1\Phi_0$ (optimal operation point, see sec. III). We again observe the 3rd harmonic is comparable to the fundamental, while the 2nd one is negligible. At higher frequencies the 3rd harmonic becomes increasingly weak, hinting at the inhibition of harmonic generation by the cut-off of the Δ mode —around 9.6 GHz.

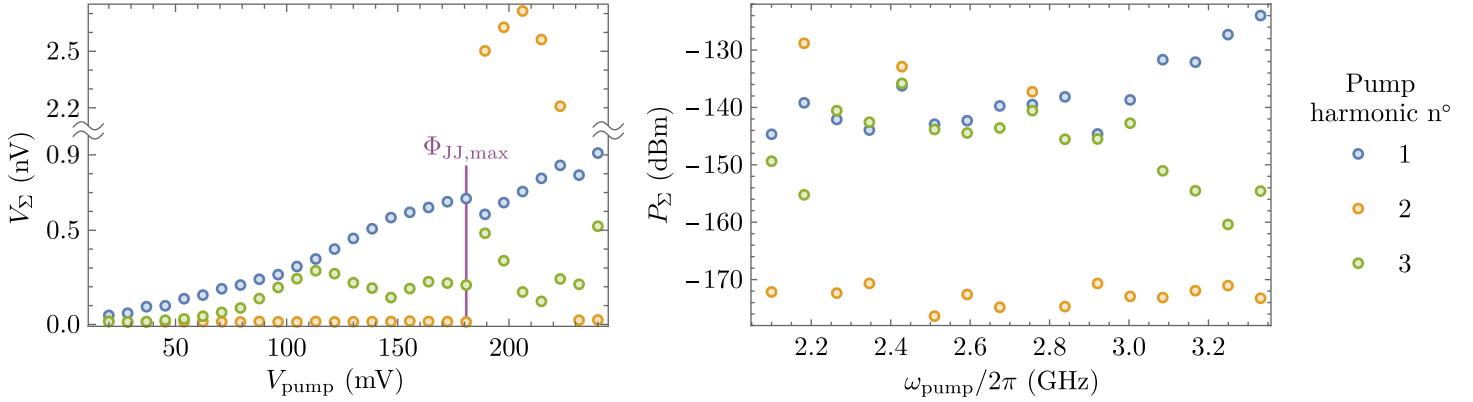


FIG. S18. **Power of the pump fundamental tone and harmonics leaking in the Σ mode.** **Left**, Harmonics for a pump at $\omega_{\text{pump}}/2\pi = 2.19$ GHz, as a function of pump amplitude. The power is expressed in terms of voltage in a 50Ω line. The 3rd harmonic (green) is detectable at all but lowest pump amplitudes. The 2nd harmonic (orange) cannot be generated by four wave mixing, hence why it is negligible except for a few outlying points at high pump amplitude. The purple $\Phi_{\text{JJ,max}}$ line indicates the optimal working amplitude (see Sec. III). **Right**, Harmonics of the pump at working amplitude of $\Phi_{\text{JJ,max}} = 0.1\Phi_0$ versus pump frequency. The 3rd harmonic is a few dBs below the fundamental for frequencies below 3GHz, and collapses above that frequency. This can be explained by the cut-off of the Δ mode at around 9.6 GHz, which inhibits harmonic generation. The 2nd harmonic is present only at a few points, showing the device works predominantly in four wave mixing.

While coincidental with the expected increase of isolation with higher frequencies, the reduced level of harmonics above a pump frequency 3.0 GHz could partially explain the device better performance in this frequency range. Harmonic suppression schemes could therefore be an improvement in a future sample. We also note the power of the pump wave traveling in the Δ mode for $\Phi_{\text{JJ,max}} = 0.1\Phi_0$ is estimated around -90 dBm. The measured level of pump power is low given the expected asymmetry

of the junctions on the chip —1% asymmetry gives $20 \log_{10}(0.01) = -40$ db of leakage.

C. Coherent detection

Spectrum analysis does not provide information about the coherence of wave conversion in the circulation process. To investigate this, we modify the original setup so that we can so that we can coherently detect converted waves with respect to the sent waves. We add down and up-conversion blocks to the left and right output lines, respectively, see Fig S19, so that the device reflections including conversion can be measured with a vector network analyzer. The mixers used are model XM-B2V1-0409C. The local oscillator (LO), intermediate frequency (IF) and radiofrequency (RF) specifications constrain the range of working points at which this coherent detection may be performed. Thus, we measure the device while applying a pump frequency of 2.19 GHz. The LO frequency is therefore at twice the pump frequency, 4.38 GHz, and generated by a source, model APUASYN20-4 from Anapico. The signal gap is around 4.4 GHz, in the IF range of the mixer, and the idler gap is at around 8.8 GHz, in the RF range.

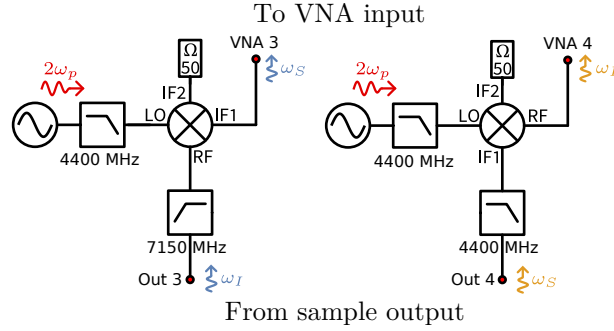


FIG. S19. **Up and down-conversion additional setup.** The point Out 3 of the left down-conversion block is inserted at the VNA 3 point in Fig S1 and the vector network analyzer is connected at the new VNA 3 point, allowing to detect wave converted to idler frequency at this output. Similarly the point Out 4 of the right up-conversion block is inserted at the VNA 4 point in Fig S1, allowing detection of waves converted to signal frequency.

Using this updated setup, we measure the conversion of the main circulating process in the relevant frequency bands (Fig S20). Signal to idler conversion is obtained from the reflection at the left Σ port of the sample, and idler to signal one from the reflection at the right Σ port of the sample. We repeat this for varying pump amplitudes. In both cases, the waves are detected against a dark background (noise floor around -90 dB) and its strength scales with the pump amplitude, confirming the coherence of the process. However, the additional uncertainty in attenuation from the up and down-conversion blocks implies quantitative verification of photon flux conservation is inaccessible with this setup.

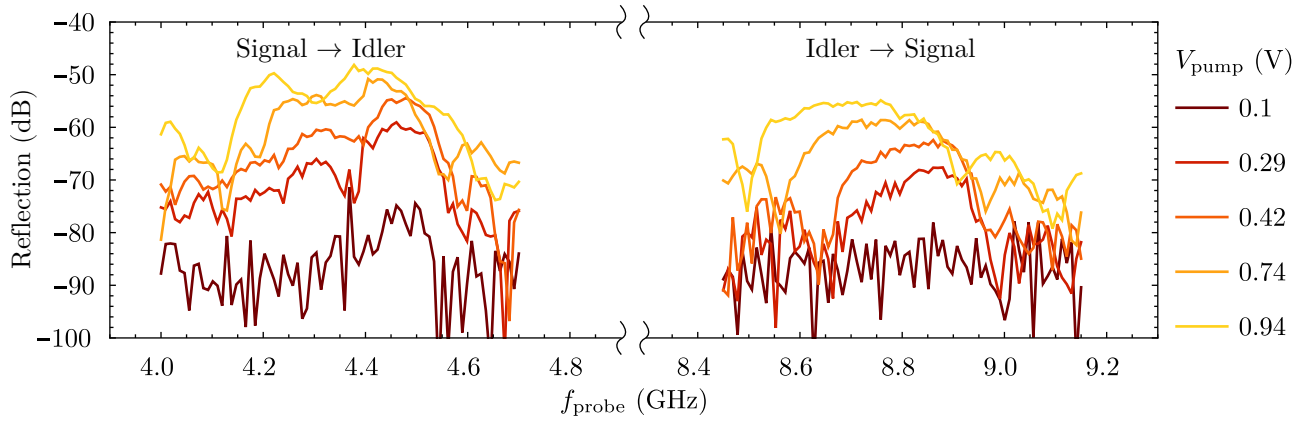


FIG. S20. **Coherent conversion detection.** A pump is sent backward at $\omega_p/2\pi = 2.19$ GHz. The left and right output lines of the Σ modes are routed to a down-conversion and up-conversion mixer setup, respectively, and then connected to the VNA (see Fig. S19). On the left (right) panel, a probe signal sent to the left (right) port at the signal (idler) frequency of the circulating process is converted to idler (signal) frequency, and is detected coherently after down-conversion (up-conversion). The colors correspond to varying pump amplitudes, showing stronger conversion with increased pump amplitude.

S8. FABRICATION RECIPE

In this section, we describe step by step the process by which our sample was fabricated.

1. Base niobium layer

- We sputter 100 nm of Nb on a 2-inch intrinsic silicon wafer, with a 275 μm thickness and a resistivity larger than 10 k.cm.
- We spin Microposit S1805 resist and pattern the base layer using optical laser lithography. We develop for 1min in Microposit MF-319.
- We etch the niobium in a Reactive Ion Etching (RIE) machine, using a SF-6 plasma, and taking great care to stop the process as soon as the exposed metal is fully removed as the silicon has a high etching rate. A steep step resulting from excessive etching could be an issue during the deposition of the final aluminum layer, preventing proper film continuity.
- We clean the wafer in a 50°C acetone, and ultrasounds for 2min, rinse in IPA for 30s, and end with a 10s O₂ plasma cleaning in the RIE machine.

2. Alumina dielectric layer

- We then deposit 80nm of alumina dielectric in a thermal Atomic Layer Deposition machine, the reactants being trimethylaluminum and water.
- We spin Microposit S1813 resist and pattern the mask for the dielectric etching using laser lithography. We develop for 1min in Microposit MF-319.
- We etch the alumina in the RIE machine, using a CHF₃ plasma.
- We clean the wafer in a 50°C acetone, and ultrasounds for 2min, rinse in IPA for 30s, and end with a 10s O₂ plasma cleaning in the RIE machine.

3. Top aluminum layer

- We coat the wafer with a bilayer of methyl methacrylate-polymethyl methacrylate (MMA EL10-PMMA A6), MMA is baked for 2min at 185°C, PMMA for 30min at 185°C, in prevision of electronic lithography. The electron beam patterning will be done at chip scale, so we coat the wafer an additional unbaked PMMA layer for protection, and then cut it into chips using a dicing saw.
- We clean individual chips in IPA, dissolving only the unbaked PMMA. We use ultrasounds for 5min.
- We pattern the Dolan bridge structure, as well as large opening for the top plate of the capacitors, using a 20keV electron beam. Note that the capacitors openings are slightly reduced compared to their desired size to compensate for the additional shadow of the later angle evaporation.

- We develop the patterned chip in a 3:1 volume IPA:water mix at 6°C for 1min30s, and we rinse it in IPA. We perform a 10s O₂ plasma cleaning in the RIE machine to clean the resist residues.
- We place the chip inside the vacuum chamber of the electron-beam evaporator. We ion-mill the surface at double angles +30°/-30°, using an argon ion gun, to prepare it for good electrical contact (7sccm flow, $V_{\text{discharge}} = 40$ V, $V_{\text{beam}} = 500$ V, $V_{\text{acc}} = 100$ V, $I = 35$ mA, 22 s duration for each angle). We deposit 35nm of aluminum at +30° angle, then oxidize the surface of the metal in a 3mbar O₂ atmosphere for 10 min (note that this low oxydation pressure explains the unusually high plasma frequency of our junctions). We finally deposit 100nm of aluminum at a -30° angle.
- We lift-off in a 50°C acetone bath for 1h, sonicate for 2min in a clean 50°C acetone bath and rinse in IPA for 30s.